Forward degenerate four-wave-mixing spectra of NO in the strong-field regime including polarization, line coupling, and multipole effects. I. Theory

V. Krüger,[1] M. Dumont,[2] S. Le Boiteux,[3] Y. J. Picard,[1] F. Chaussard,[1] and B. Attal-Trétout[1,*]

[1]*Office National d'Études et de Recherches Aérospatiales, Boîte Postale 72, 92322 Châtillon Cedex, France*
[2]*Laboratoire de Photonique Quantique et Moléculaire, École Normale Supérieure de Cachan, 61 Avenue du Président Wilson, 94235 Cachan Cedex, France*
[3]*Centre de Physique Moléculaire Optique et Hertzienne, Université de Bordeaux I, 351 cours de la Libération, 33405 Talence Cedex, France*

In the present paper, we investigate the saturation mechanism of FDFWM (forward degenerate four-wave-mixing) spectra, observed with different polarizations of the input beams, line coupling, and Doppler effect. Our theoretical approach uses a nonperturbative resolution of the density matrix equations, decomposed on the irreducible tensor basis. This formalism greatly simplifies analytical expressions and allows for a correct treatment of magnetic sublevels structure in a three-J level system. Systematic calculations of the FDFWM signal for specific NO lines are performed to characterize intensities and line shapes as a function of saturation. Relative intensities exhibit strong changes in the intermediate regime of saturation further supporting the necessity for using such a complete model. Under saturating conditions, line coupling is shown to distort the spectra, according to the type of transition and the polarization configuration. This effect is observed in the following paper [V. Krüger *et al.*, paper II, Phys. Rev. A **64**, 012717 (2001)], where saturated experimental spectra of NO are presented and interpreted for two polarization configurations of interest for diagnostic purposes.

I. INTRODUCTION

Degenerate four-wave-mixing (DFWM) spectroscopy is a widely investigated optical method, used as a diagnostic tool in reactive media. Theoretical models are required to understand the physical mechanisms involved, to evaluate the sensitivity of DFWM measurements and to interpret the experimental results. Quantitative concentration or temperature of reactive species are usually measured by fitting the experimental spectrum with the corresponding theoretical simulation. However, under saturation conditions, quantitative measurements are difficult to obtain because the relative intensities of the spectral lines are strongly modified [1]. On the other hand, this behavior can be further exploited to enhance new applications of the DFWM technique, introducing a need for accurate simulation of saturated signal.

Following these goals, different models have been developed to properly reproduce the DFWM line shape and intensity under saturated conditions. Abrams and Lind [2,3] are among the first to present a model for saturation of DFWM process in absorbing medium. Their model relies on the analytical resolution of the wave equation in the phase conjugate scheme, restricted to the steady-state and undepleted strong pump beams. They have focused on the study of the signal reflectivity for different conditions of saturation, absorption, and detuning, in order to optimize the conjugated wave. This basic approach has been used in many other developments such as the recent model of Ai and Knize [4]. These authors

have numerically solved the wave equation involving arbitrary intensities of the incident beams. They have demonstrated that optimum efficiency is achieved using equal intensities for the three beams. They have also treated the case of strong absorption and spectral line detuning, yielding to the same conclusions as Abrams and Lind in terms of optimum efficiency of the process.

In a different manner, Ducloy and co-workers [5,6] have developed a theory for DFWM, including two strong pump beams and the Doppler effect. They have solved in two ways the density matrix equation by a perturbative development of the weak probe interaction. First, they have considered a three-J level atomic system. A numerical solution of the density matrix equations is needed in this case. Second, an analytical expression is derived assuming a pair of two-level transitions on which each pump beam saturates. The results are found to be similar in line shape and intensity for either resolution whatever the saturating pump.

Using the dressed-atom formalism, Grynberg *et al.* [7,8] have analytically treated the case of one saturating quantified pump beam in a Doppler-broadened two-level state, whereas the weak beams are classically treated. Their results are compared with the preceding ones of Ducloy and give a good agreement, with simpler analytical formulas.

Focusing on the effect of laser bandwidth in saturated media, Ewart and co-workers [9–11] have established a model for two broad strong pumps and a weak narrow probe in a phase conjugate arrangement. They have resolved the time-dependent density matrix equation using a perturbative formalism on a two-level system. The problem is then simplified in a reduced number of terms. A spectral line shape including Doppler and finite bandwidth effects is obtained and the variation of efficiency is studied.

Using a different approach, Lucht *et al.* have investigated the physics of the DFWM process by direct numerical integration of the time- and space-dependent density matrix equations [12] using two-level representation. Their calculations assume a phase conjugate geometry and include three strong beams, as well as the Doppler effect. Saturated profiles obtained in a jet of NO [12] and in a flame for OH [13] have validated the calculated line shape in the saturation regime. Their calculations may account for short-pulse effects [14], closely-spaced resonances without coupling [15], polarization spectroscopy [16], and recently the forward geometry for DFWM [17]. The effects of temperature [18] and short-pulse have been discussed in the high-field limit, and applied to concentration measurements in flames and plasmas. The recent comparison of the phase conjugate and forward phase-matched geometries has shown that the signal is stronger for the forward case in condition of intermediate saturation as it was previously demonstrated for the low-field limit [19,20]. A more recent paper dealing with phase conjugate geometry tends to include the *M*-level degeneracy in the coupling scheme up to 22 levels but still disregarding reorientation effects [21].

Focusing on the experimental conditions of flame environments, two models were proposed for the DFWM forward geometry. In the first one, Attal-Trétout *et al.* [22] have applied the radiative renormalization method of Blum *et al.* [23] to the DFWM process. Analytical solutions of density matrix equations were obtained for a three-level system interacting with two strong fields and crossed-polarization scheme, which is important in the degenerate configuration. The Doppler effect is also included. A parametric study was achieved to enhance experimental feasibility. In a second model, Robertson *et al.* [24] describe the DFWM interaction in the high-field limit with a fully quantified system. It includes line coupling and the Doppler effect in different polarization configurations. It demonstrates that line coupling is specially relevant for NO DFWM spectra. The two previous models were applied to OH and NO, with due account for high intensity of the beams in flame environment. Although these simulations cover the whole saturation regime, some physical characteristics of the lines were not completely recovered. Therefore, we present here a new model that will properly reproduce the line coupling induced by the three strong incident fields as well as the different polarization schemes of the beams.

Our approach combines analytical resolution of the density matrix equations and irreducible tensor formalism in order to properly restore the saturation effects in a FDFWM (forward degenerate four-wave-mixing) process. We do account for the polarization of each incident field, the *M*-level degeneracy, and the multipole nature of the collisional parameters. In addition, the line mixing of unresolved rotational structures is taken into account by assuming a three-*J* level scheme for each line doublet (main line and its satellite).

II. THEORY

Up to now in DFWM spectroscopy, the development of density matrix over irreducible tensor operators has only

been applied to perturbative models [25–28], restricting them to the weak-field limit. This development, applied to the resolution of density matrix equations, exploits inherent symmetries of the system. Line shape function, molecular line strength as well as polarization factors are naturally included in the system. Yet, it amplifies the physical insights of the problem and allows for calculations in the strong-field regime.

It is well known that the interaction of the three waves with the molecular system generates in the medium a nonlinear polarization. It contains the source term of the DFWM signal and is here represented by the polarization operator. The theoretical mean value of any operator A is deduced from the density matrix operator ρ, using the well-known relation

$$\langle A \rangle = \mathrm{Tr}(\rho A). \tag{1}$$

where $\mathrm{Tr}(\cdots)$ is the notation for the trace operation. All the significant physical information for the system is included in the density matrix operator ρ. We therefore have to evaluate the density matrix components describing the four-wave-mixing process and apply Eq. (1) to deduce the polarization operator $\vec{P}$ responsible for the signal generation. It is related to the dipole moment operator $\vec{\mu}$ by

$$\langle \vec{P} \rangle = \mathrm{Tr}(\rho \vec{\mu}). \tag{2}$$

A. Irreducible tensor components

In order to simplify the calculation and by using the inherent symmetries of the system, it is convenient to expand ρ in terms of irreducible tensorial elements [29,30] instead of the more usual basis $|n_\alpha J_\alpha M_\alpha\rangle\langle n_\beta J_\beta M_\beta|$. In the latter, J and M, respectively, label the total angular momentum and its projection over the z axis (direction of propagation). n denotes the other quantum numbers describing the state. The density matrix is written as

$$\rho = \sum_{n_\alpha J_\alpha M_\alpha, n_\beta J_\beta M_\beta} \rho_{n_\alpha J_\alpha M_\alpha, n_\beta J_\beta M_\beta} |n_\alpha J_\alpha M_\alpha\rangle\langle n_\beta J_\beta M_\beta| \tag{3}$$

in the standard basis, and

$$\rho = \sum_{\alpha\beta, kQ} {}_{\alpha\beta}\rho_Q^k {}_{\alpha\beta}T_Q^k \tag{4}$$

in the irreducible basis, following the notation of Omont [31]. The equivalence between components is given by

$$\rho_{n_\alpha J_\alpha M_\alpha, n_\beta J_\beta M_\beta} = \sum_{k, Q} \langle n_\alpha J_\alpha M_\alpha|_{\alpha\beta}T_Q^k|n_\beta J_\beta M_\beta\rangle_{\alpha\beta}\rho_Q^k \equiv \rho_{\alpha\beta}, \tag{5}$$

where

$$\langle n_\alpha J_\alpha M_\alpha |_{\alpha\beta} T_Q^k | n_\beta J_\beta M_\beta \rangle$$

$$= (-1)^{J_\alpha - M_\alpha} \sqrt{2k+1} \begin{pmatrix} J_\alpha & k & J_\beta \\ -M_\alpha & Q & M_\beta \end{pmatrix}. \quad (6)$$

$_{\alpha\beta}T_Q^k$ is a k-rank tensor and components Q obey the conditions $-k \le Q \le k$ with $|J_\alpha - J_\beta| \le k \le J_\alpha + J_\beta$. The tensorial operator $_{\alpha\beta}T^{(k)}$ forms an orthonormalized basis of the Liouville space

$$\text{Tr} (_{\alpha\beta}T_Q^k {}_{\alpha'\beta'} T_{Q'}^{k'\dagger}) = \delta_{\alpha\alpha'} \delta_{\beta\beta'} \delta_{kk'} \delta_{QQ'} \quad (7)$$

and

$$_{\alpha\beta}T_Q^{k\dagger} = (-1)^{J_\alpha - J_\beta + Q} {}_{\beta\alpha}T_{-Q}^k. \quad (8)$$

The mean value of the irreducible tensor is calculated with Eqs. (1) and (7)

$$\langle {}_{\alpha\beta}T_Q^{k\dagger} \rangle = \text{Tr}(\rho {}_{\alpha\beta}T_Q^{k\dagger}) = {}_{\alpha\beta}\rho_Q^k \equiv \langle T(J_\alpha, J_\beta)_{kQ}^\dagger \rangle. \quad (9)$$

We introduce here the so-called state multipole $\langle T(J_\alpha, J_\beta)_{kQ}^\dagger \rangle$ defined by Blum [32].

From a physical point of view, the off-diagonal component $_{\alpha\beta}\rho_Q^k (\alpha \ne \beta)$ is the k-order multipolar coherence between states $|n_\alpha J_\alpha M_\alpha \rangle$ and $|n_\beta J_\beta M_\beta \rangle$, whereas the diagonal elements $_{\alpha\alpha}\rho_Q^k \equiv {}_\alpha \rho_Q^k$ are the orientational components of the k-order multipolar component of the molecular anisotropy of level $|n_\alpha J_\alpha \rangle$. $_\alpha\rho_0^k$ are linear combinations of the M_α populations and $_\alpha\rho_Q^k (Q \ne 0)$ are related to Zeeman coherences. The components $_\alpha\rho_Q^1$ and $_\alpha\rho_Q^2$ respectively correspond to the orientation (polar order) and alignment (quadrupolar order) of the angular momentum J_α of level $|n_\alpha J_\alpha \rangle$ [33].

Let us note that the classical definition of the density matrix where $\text{Tr}(\rho) = 1$ is not assumed in this formalism. Instead, we consider an open system where the total number of molecules may vary. The number of molecules in level $|n_\alpha J_\alpha \rangle$ per volume unit is

$$N_\alpha = \text{Tr}(\rho_{\alpha\alpha}) = \sqrt{2J_\alpha + 1} {}_\alpha \rho_0^0 = \sum_{M_\alpha} N_{n_\alpha J_\alpha M_\alpha}. \quad (10)$$

B. Density matrix formalism

The system evolution is expressed in terms of the Schrödinger equation

$$\frac{d\rho}{dt} = -\frac{i}{\hbar}[H_o + H_i, \rho] + \Lambda + \left(\frac{d\rho}{dt}\right)_{\text{rel}+\text{tr}}. \quad (11)$$

In this expression, H_o is the Hamiltonian of the unperturbed molecular system and H_i the interaction Hamiltonian of the molecules with classical electromagnetic field $\vec{E}$. In the electric dipolar approximation, $H_i = -\vec{\mu} \cdot \vec{E}$, where $\vec{\mu}$ is the electric dipole moment operator. Λ is the source term for the implementation of initial conditions. The last term

$(d\rho/dt)_{\text{rel}+\text{tr}}$ contains the phenomenological evolution of ρ along different relaxation and transfer processes.

Let us develop the interaction Hamiltonian over the irreducible representation involving $|n_\alpha J_\alpha \rangle$ and $|n_\beta J_\beta \rangle$ levels. Recognizing $\vec{\mu}$ and $\vec{E}$ as spherical tensors of rank $k=1$ and applying the Wigner-Eckart theorem, one has

$$\vec{\mu}_{\alpha\beta} \cdot \vec{E} = \frac{\mu_{\alpha\beta}}{\sqrt{3}} \sum_q (-1)^q {}_{\alpha\beta}T_q^1 E_{-q}, \quad (12)$$

with E_{-q} the irreducible component of $\vec{E}$ defined as

$$E_{\pm 1} = \mp \frac{1}{\sqrt{2}}(E_x \pm iE_y), \quad E_0 = E_z, \quad (13)$$

with z the direction of propagation, and

$$\vec{\mu}_{\alpha\beta} = \frac{\mu_{\alpha\beta}}{\sqrt{3}} {}_{\alpha\beta}T^{(1)}, \quad (14)$$

with $\mu_{\alpha\beta} = \langle n_\alpha J_\alpha \| \mu^{(1)} \| n_\beta J_\beta \rangle$. Assuming that $\mu_{\alpha\beta}$ is real, we get

$$\mu_{\beta\alpha} = (-1)^{J_\beta - J_\alpha} \mu_{\alpha\beta}. \quad (15)$$

Applying Eq. (9) to Eq. (11) leads to the equation of motion in the irreducible basis; we therefore have

$$\text{Tr}(\dot{\rho} {}_{\alpha\gamma}T_Q^{k\dagger}) = {}_{\alpha\gamma}\dot{\rho}_Q^k$$

$$= -\frac{i}{\hbar} \text{Tr}([H_o, \rho] {}_{\alpha\gamma}T_Q^{k\dagger}) + \text{Tr}\left[\left(\frac{d\rho}{dt}\right)_{\text{rel}+\text{tr}} {}_{\alpha\gamma}T_Q^{k\dagger}\right]$$

$$+ \text{Tr}(\Lambda_{\alpha\gamma}T_Q^{k\dagger}) + \frac{i}{\hbar} \text{Tr}[((\vec{\mu}_{\alpha\beta} \cdot \vec{E})\rho_{\beta\gamma}$$

$$- \rho_{\alpha\beta}(\vec{\mu}_{\beta\gamma} \cdot \vec{E})) {}_{\alpha\gamma}T_Q^{k\dagger}]. \quad (16)$$

Then using Eq. (5)

$$_{\alpha\gamma}\dot{\rho}_Q^k = i\omega_{\alpha\gamma} {}_{\alpha\gamma}\rho_Q^k + \left(\frac{d {}_{\alpha\gamma}\rho_Q^k}{dt}\right)_{\text{rel}+\text{tr}} + {}_{\alpha\gamma}\Lambda_Q^k$$

$$+ \frac{i}{\sqrt{3}\hbar} \sum_{k',Q',q} (-1)^q E_{-q}$$

$$\times [\mu_{\alpha\beta} \text{Tr}(_{\alpha\beta}T_q^1 {}_{\beta\gamma}T_{Q'}^{k'} {}_{\alpha\gamma}T_Q^{k\dagger}) {}_{\beta\gamma}\rho_{Q'}^{k'}$$

$$- {}_{\alpha\beta}\rho_{Q'}^{k'} \mu_{\beta\gamma} \text{Tr}(_{\alpha\beta}T_{Q'}^{k'} {}_{\beta\gamma}T_q^1 {}_{\alpha\gamma}T_Q^{k\dagger})], \quad (17)$$

where $\omega_{\alpha\gamma}$ is the transition frequency between $|n_\alpha J_\alpha \rangle$ and $|n_\gamma J_\gamma \rangle$. The trace is calculated with the help of Eqs. (6) and (8) as

$$\mathrm{Tr}(\,_{\alpha\beta}T^{k_1}_{q_1}{}_{\beta\gamma}T^{k_2}_{q_2}{}_{\alpha\gamma}T^{k_3\dagger}_{q_3}) = (-1)^{J_\alpha - J_\gamma + q_3}\sum_{M_\alpha M_\beta M_\gamma}\langle n_\alpha J_\alpha M_\alpha|\,_{\alpha\beta}T^{k_1}_{q_1}|n_\beta J_\beta M_\beta\rangle\langle n_\beta J_\beta M_\beta|\,_{\beta\gamma}T^{k_2}_{q_2}|n_\gamma J_\gamma M_\gamma\rangle$$

$$\times\langle n_\gamma J_\gamma M_\gamma|\,_{\gamma\alpha}T^{k_3}_{-q_3}|n_\alpha J_\alpha M_\alpha\rangle$$

$$= \sqrt{(2k_1+1)(2k_2+1)(2k_3+1)}(-1)^{2J_\beta - J_\alpha + J_\gamma + q_3}\begin{pmatrix} k_2 & k_1 & k_3 \\ q_2 & q_1 & -q_3 \end{pmatrix}\begin{Bmatrix} k_1 & k_2 & k_3 \\ J_\gamma & J_\alpha & J_\beta \end{Bmatrix}. \quad (18)$$

And we finally get

$$_{\alpha\gamma}\dot\rho^k_Q = i\omega_{\alpha\gamma}{}_{\alpha\gamma}\rho^k_Q - \left(\frac{d\,_{\alpha\gamma}\rho^k_Q}{dt}\right)_{\mathrm{rel+tr}} + {}_{\alpha\gamma}\Lambda^k_Q - \sum_{k'Q'q}\frac{i}{\hbar}(-1)^{q+Q+J_\alpha}\sqrt{(2k+1)(2k'+1)}\,\mathbf{E}_{-q}\begin{pmatrix} k' & 1 & k \\ Q' & q & -Q \end{pmatrix}$$

$$\times\left(\begin{Bmatrix} k' & 1 & k \\ J_\alpha & J_\gamma & J_\beta \end{Bmatrix}\mu_{\alpha\beta}{}_{\beta\gamma}\rho^{k'}_{Q'} + (-1)^{k+k'}\begin{Bmatrix} k' & 1 & k \\ J_\gamma & J_\alpha & J_\beta \end{Bmatrix}{}_{\alpha\beta}\rho^{k'}_{Q'}\mu_{\beta\gamma}\right). \quad (19)$$

This last equation is valid whatever the geometrical configuration if no permanent electric or magnetic field is present. It fully incorporates the coupling of degenerate magnetic sublevels *M* inside each rotational level through the sum over k' and Q'. To apply it to FDFWM process in a gas-phase medium described by a three-*J* level system, we have to take into account the experimental configuration.

C. Beam and polarization configuration

Unlike many DFWM simulations in phase-conjugate beam geometry, the present model is concerned with the folded-Boxcars geometry in which the three incident beams are traveling in the forward direction along *z* axis as shown in Fig. 1. The subscripts 1, 2, and 3 refer to the three incident beams, and index 4 represents the signal beam. For linear polarizations of the incident beams and a *y*-polarized signal, the different possible polarization arrangements are set in Fig. 2. They are respectively labeled along the *y* or *x* polarization direction, in the conventional order $\hat\epsilon_4\hat\epsilon_1\hat\epsilon_3\hat\epsilon_2$ [34]. The *yyyy* polarization is called the all-parallel case. The crossed-polarizations *yyxx* and *yxyx* are equivalent in the forward box [20]. In Fig. 2, the different types of gratings induced by the pump-probe interference have been outlined in order to recognize the population and polarization gratings respectively shown as shaded and dotted ellipse.

We assume plane and degenerated monochromatic waves and a free propagation of the fields in the medium along the *z* axis. The total incident field $\vec{\mathbf{E}}$ is the sum of the three incident fields that may have arbitrary unequal individual intensities.

$$\vec{\mathbf{E}} = \tfrac{1}{2}(\vec{\mathsf{E}} + \vec{\mathsf{E}}^*)$$

$$\vec{\mathsf{E}} = \sum_{i=1,2,3}\vec{\mathsf{E}}_i$$

$$\vec{\mathsf{E}}_i = \hat\epsilon_i E_i e^{i(\vec{k}_i\cdot\vec{r} - \omega t)}$$

$$\text{with}\quad \vec{E}_i \equiv \hat\epsilon_i E_i \quad (20)$$

where the electric field $\vec{\mathsf{E}}_i$ for $i=1,2,3$ is specified by its polarization vector $\hat\epsilon_i$, its frequency ω, its wave vector $\vec{k}_i$, and its scalar amplitude E_i.

The polarization vector $\hat\epsilon_i$ is expanded either on a real orthonormal basis $(\hat{e}_x, \hat{e}_y, \hat{e}_z)$ or on a complex spherical tensor basis defined as follows

$$\hat{e}_{\pm1} = \mp\frac{1}{\sqrt{2}}(\hat{e}_x \pm i\hat{e}_y), \quad \hat{e}_0 = \hat{e}_z, \quad (21)$$

with the following properties

$$\hat{e}^*_q = (-1)^q\hat{e}_{-q}, \quad \hat{e}_q\cdot\hat{e}^*_{q'} = \delta_{qq'}. \quad (22)$$

The three beams are crossing with a very small angle ($\approx 1°$), so that it is a good approximation to assume almost collinear beams. The *z* component of all electric fields is
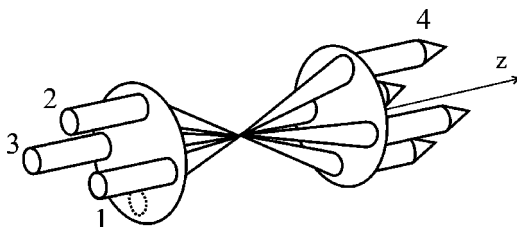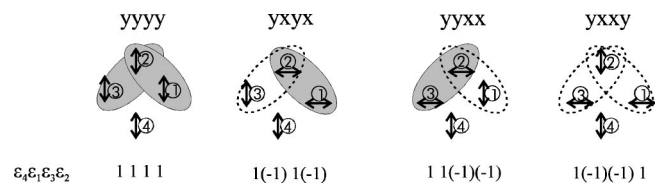

FIG. 1. Beam configuration: folded Boxcars.

yyyy	yxyx	yyxx	yxxy

$\epsilon_4\epsilon_1\epsilon_3\epsilon_2$ 1 1 1 1   1(-1) 1(-1)   1 1(-1)(-1)   1(-1)(-1) 1

FIG. 2. Different linear polarization arrangements and related ε_i values defined in Eqs. (29) according to the labeling $\hat\epsilon_4\hat\epsilon_1\hat\epsilon_3\hat\epsilon_2$.

negligible and we will assume that all their polarization vectors are in the (x,y) plane. Therefore, each field is developed on either basis, leading to

$$\vec{E}_i = (E_i)_x \hat{e}_x + (E_i)_y \hat{e}_y = (E_i)_+ \hat{e}_{+1}^* + (E_i)_- \hat{e}_{-1}^* \quad (23)$$

and according to Eq. (13)

$$(E_i)_\pm = \mp \frac{1}{\sqrt{2}}[(E_i)_x \pm i(E_i)_y]. \quad (24)$$

It is further simplified

$$(E_i)_\pm = \mp \frac{1}{\sqrt{2}} E_i = e^{i\pi}\left(\pm \frac{1}{\sqrt{2}} E_i\right) \quad (25)$$

for polarization along x and

$$(E_i)_\pm = -\frac{i}{\sqrt{2}} E_i = e^{-i(\pi/2)}\left(\frac{1}{\sqrt{2}} E_i\right) \quad (26)$$

for polarization along y. The relative phase of the three input beams is not important, merely resulting in a translation of the space and time origin. Thus changes of little importance can be performed on the phase factor to simplify these expressions. For linear polarization, we can finally write Eqs. (25) and (26) as

$$(E_i)_\pm = \pm \frac{1}{\sqrt{2}} E_i \quad (27)$$

for polarization along x and

$$(E_i)_\pm = \frac{1}{\sqrt{2}} E_i \quad (28)$$

for polarization along y. Note that in this configuration, the contribution to $(E_i)_\pm$ is always real and $(E_i)_+$ is positive.

According to the geometry of Fig. 3, we define the following wave-vector projections $k_x = -(k_1)_x = (k_3)_x$, $k_y = -(k_2)_y$, and $k_z = (k_i)_z$ with $k_x, k_y \ll k_z$. Introducing the phase vector $\exp(i\vec{k}_i \cdot \vec{r})$, the total electric field components in the spherical basis are written as follows:

$$E_+ = \frac{1}{\sqrt{2}}\{E_1 e^{-ik_x x} + E_2 e^{-ik_y y} + E_3 e^{ik_x x}\} e^{i(k_z z - \omega t)}$$

$$\equiv \mathcal{E}_+ e^{-i\omega t} \equiv E_+ e^{i\varphi_+} e^{-i\omega t}, \quad (29a)$$

$$E_- = \frac{1}{\sqrt{2}}\{\varepsilon_1 E_1 e^{-ik_x x} + \varepsilon_2 E_2 e^{-ik_y y} + \varepsilon_3 E_3 e^{ik_x x}\} e^{i(k_z z - \omega t)}$$

$$\equiv \mathcal{E}_- e^{-i\omega t} \equiv E_- e^{i\varphi_-} e^{-i\omega t}, \quad (29b)$$

with $\varepsilon_i = -1$ for x polarization, and $\varepsilon_i = +1$ for y polarization for $i = 1,2,3$. Depending on the polarization arrangement of the incident laser beams, the input parameters ε_i are dif-

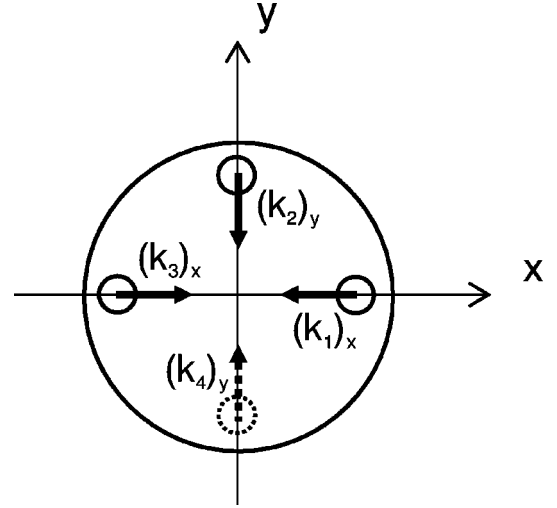FIG. 3. Transversal section of the four interacting beams, exhibiting wave-vector projections.

ferent (Fig. 2). The quantities $E_\pm$ and $\varphi_\pm$ are all depending on x, y, and z. They represent the interference pattern of the three beams.

The total phase factor of $E_\pm$ is split between the spatial one $\varphi_\pm$ and the temporal one as shown in Eqs. (29). This allows a simplification of $\varphi_\pm$ that depends on spatial position[1]

$$\varphi_\pm = \frac{\varphi_+ + \varphi_-}{2} \pm \frac{\varphi_+ - \varphi_-}{2} = \varphi_0 \pm \psi. \quad (30)$$

A rotation of the axes used for describing the polarization, by the angle $\psi = (\varphi_+ - \varphi_-)/2$ around the z axis, leads to new components of the field given by

$$\tilde{\mathcal{E}}_\pm = E_\pm e^{i\varphi_0}. \quad (31)$$

The phase factor φ_0 is then the same for both components and can be suppressed in the equations by a simple change of the time origin. At this stage, according to this phase simplification, the field expressions of Eqs. (29) are introduced into Eq. (19) with

$$\mathbf{E}_{q=\pm 1} \equiv \mathbf{E}_\pm = \tfrac{1}{2}(E_\pm e^{-i\omega t} - E_\mp e^{i\omega t}). \quad (32)$$

The position-dependent phase factors are reintroduced at the end of the resolution (see Sec. II G) in the expression of the signal polarization

$$\mathbf{P}_\pm^{\text{final}} = e^{i\varphi_0}\mathbf{P}_\pm e^{\pm i\psi} = \mathbf{P}_\pm e^{i\varphi_\pm}. \quad (33)$$

These phase factors reflect the coherent features of the incident-field polarizations into the final calculation of **P**. To

_____

[1]We define a new local axis in order to simplify the equation of the polarization. Nevertheless, x and y axes are still valid to define the wave vector $\vec{k}_i$ and the position of each point.
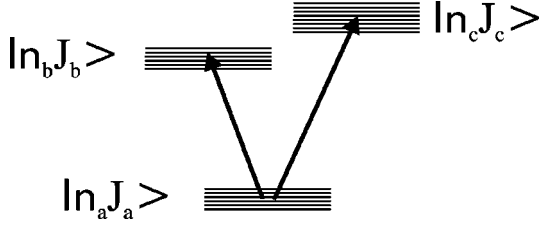
FIG. 4. Three-J level scheme of main $|a\rangle \rightarrow |b\rangle$ and satellite $|a\rangle \rightarrow |c\rangle$ transitions.

account for these coherent effects, an integration of Eq. (33) is performed on the spatial coordinates as described in Sec. II H.

D. Collisional modeling

The collisional rates of the molecular system are expressed by the relaxation and transfer term of Eq. (11). The multipolar term $(d_{\alpha\gamma}\rho_Q^k/dt)_{\text{rel+tr}}$ of Eq. (19) is its projection on the $_{\alpha\beta}T^{(k)}$ basis. Because of the isotropy of relaxation and transfer processes, relaxation rates $[\Gamma(k)]$ and transfer rates $[\Theta(k)]$ do not couple tensorial components of different multipolar order. Moreover, $\Gamma(k)$ and $\Theta(k)$ do not depend on Q [30].

In the three-J level scheme, $|a\rangle$ represents the rotational ground level $|n_a J_a\rangle$; $|b\rangle$ and $|c\rangle$ respectively represent the excited levels $|n_b J_b\rangle$ and $|n_c J_c\rangle$ (Fig. 4). In the NO doublet structure, $|a\rangle \rightarrow |b\rangle$ and $|a\rangle \rightarrow |c\rangle$ correspond respectively to the main and satellite transitions originating from a common level $|a\rangle$. Relaxation of diagonal and off-diagonal components of the multipolar term are yet given by

$$\left(\frac{d_a\rho_Q^k}{dt}\right)_{\text{rel+tr}} = -\Gamma_a(k)\,_a\rho_Q^k + \Theta_{ab}(k)\,_b\rho_Q^k + \Theta_{ac}(k)\,_c\rho_Q^k$$

$$(34a)$$

$$\left(\frac{d_b\rho_Q^k}{dt}\right)_{\text{rel+tr}} = -\Gamma_b(k)\,_b\rho_Q^k + \Theta_{bc}(k)\,_c\rho_Q^k \quad (34b)$$

$$\left(\frac{d_{ab}\rho_Q^k}{dt}\right)_{\text{rel+tr}} = -\Gamma_{ab}(k)\,_{ab}\rho_Q^k \quad (34c)$$

$$\left(\frac{d_{bc}\rho_Q^k}{dt}\right)_{\text{rel+tr}} = -\Gamma_{bc}(k)\,_{bc}\rho_Q^k. \quad (34d)$$

The corresponding c, cb, and ac components are obtained by interchanging index b with c in the former expressions. The notations introduced in Eqs. (34) are defined according to [35].

$\Gamma_\alpha(k=0)$ is the population relaxation rate of the rotational level $|\alpha\rangle$, i.e., the departure toward other levels is either by spontaneous emission or by collisional transfer. $\Gamma_\alpha(k>0)$ contains in addition the effect of collisional reorientation of the angular momentum J_α. Therefore, $\Gamma_\alpha(k>0) \geqslant \Gamma_\alpha(k=0)$ with the equality fulfilled in the absence of collisions.

$\Gamma_{a\beta}$ for $\beta = b,c$, is the multipolar dephasing rate or the transverse relaxation rate. Γ_{bc} is commonly labeled a Raman linewidth and may be involved in the so-called Raman term of the density matrix equations.

The pure dephasing contributions to the linewidth $\Gamma_{\alpha\beta}$ are commonly given by the quantity

$$\Gamma_{\alpha\beta}^{\phi}(k) = \Gamma_{\alpha\beta}(k) - \tfrac{1}{2}[\Gamma_\alpha(k=0) + \Gamma_\beta(k=0)]. \quad (35)$$

The transfer rate $\Theta_{\beta\alpha}(k)$ is related to direct population and Zeeman coherence transfer from $|\alpha\rangle$ to $|\beta\rangle$, through collisions and spontaneous emission.

E. Final derivation of the equation set

The expressions of the electric field, the relaxation and transfer terms are now included in Eq. (19). The nonlinear polarization is calculated by developing the density matrix components $_{ab}\rho_Q^k$ and $_{ac}\rho_Q^k$. We first solve the density matrix equations for a single class of molecular velocity $\vec{v}$, that is for the Doppler-shifted laser frequency $\omega = \omega_{\text{laser}} - \vec{k} \cdot \vec{v}$. Then the resolution of the system is fully performed for all velocity classes just by changing the laser frequency step by step. In this treatment, we assume a monochromatic laser emission [11]. Numerical integration of the solution over a Maxwell-Boltzmann distribution function is performed in a second step. This part of the calculation deals with complex amplitudes of the DFWM signal, which are added to reproduce the rotational structure of the spectra [20]. At this step of the calculation, the signal intensity can be calculated (squared complex amplitude) and convoluted by the laser linewidth function that is measured experimentally. This last step will be calculated effectively in paper II [1] where comparison with experiments is required.

We use the rotating wave approximation (RWA) that consists in keeping only the nearly resonant contribution into each density matrix component: $_a\rho_Q^k$, $_b\rho_Q^k$, $_c\rho_Q^k$, and $_{bc}\rho_Q^k$ are constant with time but $_{ab}\rho_Q^k$ and $_{ac}\rho_Q^k$ oscillate at the frequency $\omega \approx \omega_{ab} \approx \omega_{ac}$ since harmonic contributions are neglected. This approximation leads to $_{ab}\rho_Q^k(t) = _{ab}\rho_Q^k e^{i\omega t}$ and $_{ac}\rho_Q^k(t) = _{ac}\rho_Q^k e^{i\omega t}$. The following equations only deal with the complex amplitudes $_{ab}\rho_Q^k$ and $_{ac}\rho_Q^k$ since temporal phase factor is simplified.

The source term Λ can be calculated considering that the system is isotropic in the absence of field. Thus $_{\alpha\gamma}\Lambda_Q^k$ is only nonzero for $k=0$ and $\alpha = \gamma$. Applying Eq. (19) with $\mathbf{E} = 0$ leads to

$$_a\Lambda_0^0 = \Gamma_a(0)\rho_a^{(o)} - \Theta_{ab}(0)\rho_b^{(o)} - \Theta_{ac}(0)\rho_c^{(o)}, \quad (36a)$$

$$_b\Lambda_0^0 = \Gamma_b(0)\rho_b^{(o)} - \Theta_{bc}(0)\rho_c^{(o)}, \quad (36b)$$

where

$$\rho_\alpha^{(o)} = \,_a\rho_0^0(\mathbf{E} = 0) = N_\alpha^{(o)}/\sqrt{2J_\alpha + 1}. \quad (37)$$

$N_\alpha^{(o)}$ is the initial population of level $|\alpha\rangle$ defined as $Nn_\alpha^{(o)}$, where N is the total number density and $n_\alpha^{(o)}$ is the population fraction of level $|n_\alpha J_\alpha\rangle$ given by the normalized Boltz-

mann exponential. The temperature dependence is included in both $n_\alpha^{(o)}$ and N. N is assumed to be constant in the theoretical studies. Equations (36) allow the elimination of Λ in Eq. (19).

The stationary solution is valid when the laser pulse is long enough compared to the lifetime of the molecular levels in the collisional and Doppler regime of interest in our case. This solution is given by the following set of equations:

$$\Gamma_a(k)(\,_a\rho_Q^k - \rho_a^{(o)}\delta_{k,0}) = \Theta_{ab}(k)(\,_b\rho_Q^k - \rho_b^{(o)}\delta_{k,0}) + \Theta_{ac}(k)(\,_c\rho_Q^k - \rho_c^{(o)}\delta_{k,0}) + \frac{i}{2\hbar}\sum_{k'Q'q}(-1)^{q+Q+2J_a}\sqrt{(2k+1)(2k'+1)}$$

$$\times \begin{pmatrix} k' & 1 & k \\ Q' & q & -Q \end{pmatrix}\left[\begin{pmatrix} k' & 1 & k \\ J_a & J_a & J_b \end{pmatrix}[(-1)^q E_q \mu_{ab\,ba}\rho_{Q'}^{k'} + (-1)^{k+k'}E_{-q\,ab}\rho_{Q'}^{k'}\mu_{ba}]\right.$$

$$\left. + \begin{pmatrix} k' & 1 & k \\ J_a & J_a & J_c \end{pmatrix}[(-1)^q E_q \mu_{ac\,ca}\rho_{Q'}^{k'} + (-1)^{k+k'}E_{-q\,ac}\rho_{Q'}^{k'}\mu_{ca}]\right], \tag{38a}$$

$$\Gamma_b(k)(\,_b\rho_Q^k - \rho_b^{(o)}\delta_{k,0}) = \Theta_{bc}(k)(\,_c\rho_Q^k - \rho_c^{(o)}\delta_{k,0}) + \frac{i}{2\hbar}\sum_{k'Q'q}(-1)^{q+Q+2J_a}\sqrt{(2k+1)(2k'+1)}\begin{pmatrix} k' & 1 & k \\ Q' & q & -Q \end{pmatrix}$$

$$\times \begin{pmatrix} k' & 1 & k \\ J_b & J_b & J_a \end{pmatrix}[E_{-q}\mu_{ba\,ab}\rho_{Q'}^{k'} + (-1)^{k+k'+q}E_q\,_{ba}\rho_{Q'}^{k'}\mu_{ab}], \tag{38b}$$

$$[\omega_{bc} - i\Gamma_{bc}(k)]\,_{bc}\rho_Q^k = \frac{1}{2\hbar}\sum_{k'Q'q}(-1)^{q+Q+J_b+J_c}\sqrt{(2k+1)(2k'+1)}\begin{pmatrix} k' & 1 & k \\ Q' & q & -Q \end{pmatrix}$$

$$\times\left[\begin{pmatrix} k' & 1 & k \\ J_b & J_c & J_a \end{pmatrix}E_{-q}\mu_{ba\,ac}\rho_{Q'}^{k'} + (-1)^{k+k'+q}\begin{pmatrix} k' & 1 & k \\ J_c & J_b & J_a \end{pmatrix}E_q\,_{ba}\rho_{Q'}^{k'}\mu_{ac}\right], \tag{38c}$$

$$[\omega - \omega_{ab} - i\Gamma_{ab}(k)]\,_{ab}\rho_Q^k = \frac{1}{2\hbar}\sum_{k'Q'q}(-1)^{Q+J_a+J_b}\sqrt{(2k+1)(2k'+1)}E_q\begin{pmatrix} k' & 1 & k \\ Q' & q & -Q \end{pmatrix}$$

$$\times\left[\begin{Bmatrix} k' & 1 & k \\ J_a & J_b & J_b \end{Bmatrix}\mu_{ab\,b}\rho_{Q'}^{k'} + (-1)^{k+k'}\begin{Bmatrix} k' & 1 & k \\ J_b & J_a & J_a \end{Bmatrix}\,_a\rho_{Q'}^{k'}\mu_{ab} + \begin{Bmatrix} k' & 1 & k \\ J_a & J_b & J_c \end{Bmatrix}\mu_{ac\,cb}\rho_{Q'}^{k'}\right]. \tag{38d}$$

The equations for $_c\rho_Q^k$ and $_{ac}\rho_Q^k$ are obtained by exchanging b and c in Eq. (38b) and Eq. (38d). Here, due to the RWA approximation, the temporal phase factors of the electric field have been removed, and the equations only depend on the real amplitudes $E_\pm$ in each point. The only nonzero relations have to satisfy the triangular inequalities between J_a, J_b, J_c, and the k values. Q is odd for $_{ab}\rho_Q^k$ and even for $_a\rho_Q^k$ and $_{bc}\rho_Q^k$, because $q = \pm 1$ and because the initial state is isotropic (only $_a\rho_0^0$ is nonzero as $\mathbf{E} = 0$).

Using the relation

$$_{\alpha\beta}\rho_Q^k = (-1)^{J_\alpha - J_\beta + Q}\,_{\beta\alpha}\rho_{-Q}^{k*}, \tag{39}$$

we first eliminate $_a\rho_Q^k$ and $_{bc}\rho_Q^k$ and reduce this system of seven equations to a set of two equations involving only $_{ab}\rho_Q^k$ and $_{ac}\rho_Q^k$ components. This set is then developed for each k and Q value and the result is shown in Appendix A. It is finally written as a product of a matrix $\mathfrak{M}$ with a vector ϱ such that $\mathfrak{M}\varrho = \varrho^{(o)}$. The real and imaginary parts of $_{ab}\rho_Q^k$

and $_{ac}\rho_Q^k$ are the vector components of ϱ and $\varrho^{(o)}$ is the vector of the source term for the initial conditions. The matrix is numerically inverted and we get the solutions $\varrho = \mathfrak{M}^{-1}\varrho^{(o)}$. The dipolar terms $_{ab}\rho_Q^1$ and $_{ac}\rho_Q^1$ are derived in order to calculate the signal polarization $\mathcal{P}$ resulting from the four-wave-mixing interaction.

Let us note that an initial anisotropy of the medium could have been easily included in our calculations. Vaccaro et al. [26,27] have introduced it in their perturbative treatment by developing the initial $\rho_\alpha^{(o)}$ as a sum of irreducible tensorial elements as in Eq. (5). Furthermore, the values of $_a\rho_Q^k$, $_b\rho_Q^k$, and $_c\rho_Q^k$ for $k = 0,1,2$ could also provide information on the anisotropy of the medium after the interaction, if these values are extracted from the set of equations.

At this step of the calculation, ρ still depends on the velocity v of the molecules, on the laser frequency, and on the spatial position in the interaction volume. To get the final signal polarization generated in the phase-matched direction, integrations over the velocity distribution, the spatial coordi-

nates, and the laser bandwidth are performed as explained in the following.

This analysis treats the coupling between J and M levels and finally ends with different contributions from molecular and geometrical factors. This factorization was already introduced in the J-M basis set in a previous work [20]. The geometrical factors are expressed as products of 3-j and 6-j symbols. The above spherical tensor formalism provides a framework that takes more properly into account the reorienting collisions and the symmetry of the media. In addition, this treatment allows us to properly calculate saturation effects in forward DFWM with due account for the configuration of the incident beam polarizations [28].

F. Integration over the velocity distribution

The signal results from the contributions of all the different velocity groups, assuming a Maxwell-Boltzmann distribution. The most probable velocity u of the molecules for a given temperature T is

$$u = \left(\frac{2 \mathcal{N}_a k_B T}{m} \right)^{1/2}, \qquad (40)$$

where $\mathcal{N}_a$ is the Avogadro number, k_B the Boltzmann constant, and m the mass of the target molecule. As in previous papers [20,22], we proceed to an integration of the density matrix components $_{ab}\rho_Q^1$ and $_{ac}\rho_Q^1$ over the velocity distribution. Since the angle between the beams is very small, the Doppler effect can be neglected in the transverse direction $(k_x v_x, k_y v_y \ll \Gamma_{ab})$. We only perform the numerical integration along v_z with $k_z = k_n = n\omega/c$ and n the refractive index.

$$\langle _{ab}\rho_Q^1 \rangle_{av} = \int _{ab}\rho_Q^1(\omega_{laser} - k_n v) F(v) dv, \qquad (41)$$

with

$$F(v) = \frac{1}{u \sqrt{\pi}} e^{-(v/u)^2}. \qquad (42)$$

G. Spatial polarization

The polarization of the signal is given by its components

$$\mathcal{P}_Q(\vec{r}) = \frac{\mu_{ab}}{\sqrt{3}} \langle _{ab}\rho_Q^{1*}(\vec{r}) \rangle_{av} + \frac{\mu_{ac}}{\sqrt{3}} \langle _{ac}\rho_Q^{1*}(\vec{r}) \rangle_{av}, \quad Q = \pm 1. \qquad (43)$$

At this stage, phase factors defined in Sec. II C are reintroduced according to Eq. (33). For a signal polarized along x or y, one has

$$\mathcal{P}_x(\vec{r}) = 1/\sqrt{2}[\mathcal{P}_-(\vec{r}) - \mathcal{P}_+(\vec{r})], \qquad (44a)$$

$$\mathcal{P}_y(\vec{r}) = i/\sqrt{2}[\mathcal{P}_-(\vec{r}) + \mathcal{P}_+(\vec{r})]. \qquad (44b)$$

H. Expression of the integral over spatial coordinates

We search for the observed signal field in the phase-matched direction, far from the interaction volume. The total electric field E and the corresponding macroscopic induced polarization P are related by the wave equation

$$\frac{\partial^2 \mathsf{E}(\vec{r},t)}{\partial r^2} - \frac{n^2}{c^2} \frac{\partial^2 \mathsf{E}(\vec{r},t)}{\partial t^2} = \frac{1}{\varepsilon_o c^2} \frac{\partial^2 \mathsf{P}(\vec{r},t)}{\partial t^2}, \qquad (45)$$

where ε_o is the permittivity of vacuum, n the refractive index, and c the speed of light in the vacuum.

For sake of simplicity, we consider homogeneous plane waves. The Fourier spectrum of the polarization is constituted of discrete spatial frequencies. Keeping the only phase-matched components, one has

$$\mathcal{P}(x,y,z) = P_{-10}^{(1)} e^{i(k_1)_x x} e^{i(k_1)_z z} + P_{0-1}^{(2)} e^{i(k_2)_y y} e^{i(k_2)_z z}$$
$$+ P_{10}^{(3)} e^{i(k_3)_x x} e^{i(k_3)_z z} + P_{01}^{(4)} e^{i(k_4)_y y} e^{i(k_4)_z z}, \qquad (46)$$

where $P_{ql}^{(i)}$ is the polarization amplitude of the beam i with the wave vector (qk_x, lk_y, k_z). $P_{01}^{(4)}$ is the only component of interest for the DFWM signal, provided the solid angle of the detector is restricted around $\vec{k}_4$ direction. It means that the angle between the beams is small. So, for mathematical simplicity, we assume that the active medium is a cylinder of section S and length L parallel to $\vec{k}_4$. Because of the periodicity, $P_{01}^{(4)}$ can be calculated as a single spatial period in the interaction volume

$$P_{01}^{(4)} = \frac{k_x k_y k_z}{8\pi^3} \int_0^{2\pi/k_x} \int_0^{2\pi/k_y} \int_0^{2\pi/k_z} \mathcal{P}(x,y,z)$$
$$\times \exp\{-i[(k_4)_z z + (k_4)_y y]\} dx\, dy\, dz. \qquad (47)$$

Taking the z axis along $\vec{k}_4$, we also make the slowly varying envelope approximation. We have

$$\mathsf{E}(\vec{r},t) = \mathcal{E}(z) e^{i(k_n z - \omega t)}, \qquad (48)$$

$$\mathsf{P}(\vec{r},t) = P_{01}^{(4)} e^{i(k_n z - \omega t)}, \qquad (49)$$

with

$$\lambda \frac{d\mathcal{E}(z)}{dz} \ll 1 \quad \text{and} \quad k_n = \frac{n\omega}{c}.$$

Neglecting second derivative of $\mathcal{E}(z)$, Eq. (45) leads to

$$\frac{d\mathcal{E}(z)}{dz} = i \frac{k_n}{2\varepsilon} P_{01}^{(4)}, \qquad (50)$$

$$\mathcal{E}(L) = i \frac{k_n}{2\varepsilon} P_{01}^{(4)} L. \qquad (51)$$

The total power of the diffracted beam is

$$I_{\text{Sig}} = S\frac{\varepsilon c}{2n}|\mathcal{E}(L)|^2 = \frac{SL^2 k_n^2 c}{8\varepsilon n}|P_{01}^{(4)}|^2. \qquad (52)$$

We have made the rather crude approximation of plane waves. In Appendix B, we develop a rigorous expression that is able to take into account the real shape of the beams, for instance the crossing of Gaussian beams.

In the theoretical spectra, we plot $P_{\text{Sig}} = \sqrt{I_{\text{Sig}}}$ as a function of the parameters of interest

$$P_{\text{Sig}} = k_n L \sqrt{\frac{Sc}{8\varepsilon n}}|P_{01}^{(4)}|. \qquad (53)$$

Finally the finite width of the exciting laser is taken into account by convoluting a gaussian profile with the signal intensity I_{Sig}. This Gaussian line shape depends on the laser properties and is measured experimentally.

DFWM signals will be calculated using Eq. (54) in any range of saturation in order to interpret the NO spectra of paper II [1].

III. THE NO MOLECULE

The model presented here is applied to the particular case of NO, and is validated in flame environments (see paper II, Ref. [1]). The calculations developed in the previous section are not restricted to NO. The application to other molecules of interest such as OH and CH is straightforward, since the electronic transition involved is also a $^2\Sigma$-$^2\Pi$ one [36].

In this section, spectroscopic properties relative to NO are recalled. The transition moments are detailed according to the structure of the γ-system. The collisional widths are further simplified using the data from literature and the dynamical conditions relevant to our experimental conditions. We assume that excited electronic states are not initially populated whatever the temperature. All the following spectra are relevant to these NO data and the saturation effects observed on peculiar sets of line doublets (main and satellite).

A. Spectroscopy

The $^2\Sigma$-$^2\Pi$ electronic system of NO is composed of P, Q, and R branches. The spin-orbit coupling further decomposes the spectrum into two series of components corresponding to F_i rotational sublevels with $i=1,2$ [36–38,20,24]. The structure of the NO γ-system is illustrated in Fig. 5 and in Table I. The line labeling $^{\Delta N}\Delta J_{ij}$ ($i=1,2$) is conventional [36] and fully determines the type of transition.

In opposition to OH and CH, the main and satellite lines are nearly superimposed in NO [39]. Therefore, each rotational line is a so-called Λ doublet that can experience a particular type of coupling under strong-field excitation. NO is a characteristic molecule since the splitting between the $|b\rangle$ and $|c\rangle$ levels is very small in the $^2\Sigma$ state (<0.01 cm^{-1}) and produces coupling effects evident even in moderate conditions of saturation.
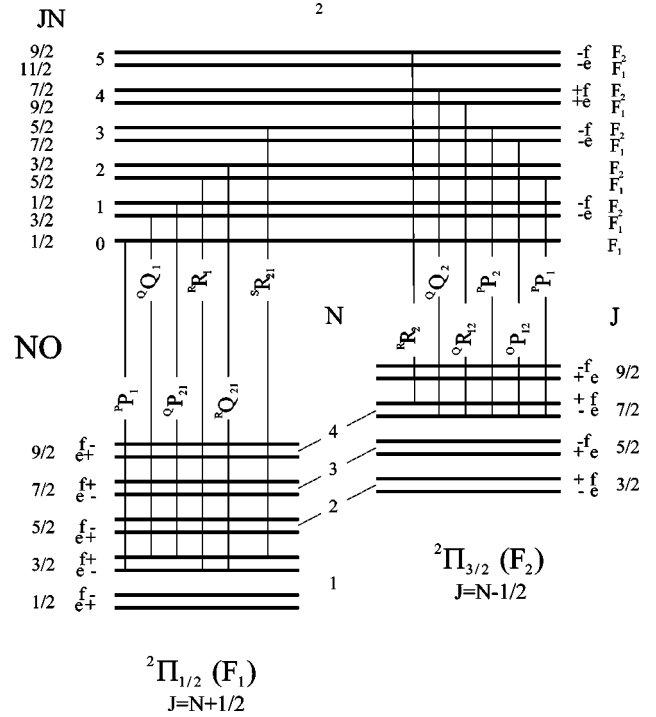

FIG. 5. Energy level diagram of the $\tilde{A}\,^2\Sigma^+$-$\tilde{X}\,^2\Pi$ electronic transition of NO. Twelve branches are defined by the parity-assigned sublevels in the $\Pi_{3/2}$ and $\Pi_{1/2}$ spin components.

B. Dipole moment description

The one-photon transition probability between $|\alpha\rangle$ and $|\beta\rangle$ is commonly defined as

$$\mathsf{S}_{\alpha\beta} = |\langle n_\alpha J_\alpha\|\mu^{(1)}\|n_\beta J_\beta\rangle|^2 = |\mu_{\alpha\beta}|^2 = (Re)^2|\langle v_\alpha|v_\beta\rangle|^2 \mathsf{S}_{\alpha\beta}^{\mathsf{J}}, \qquad (54)$$

also called molecular line strength [28]. In the Born-Oppenheimer approximation, $\mathsf{S}_{\alpha\beta}$ is expressed as the product of the Franck-Condon factors $|\langle v_\alpha|v_\beta\rangle|^2$ with the square of the electronic transition moment Re and with the Hönl-London factor $\mathsf{S}_{\alpha\beta}^{\mathsf{J}}$. This last factor is also called the rotational line strength [40]. It is calculated with Earls's values [41] and derived in Tables 5 and 8 of [24]. We treat the coupling of angular momentum with spin and rotation as an intermediate Hund's case (a–b) in the $^2\Pi$ state [36].

TABLE I. Main and satellite transitions $^{\Delta N}\Delta_J$ of the γ system of NO originating from J_a.

Main	Satellite	J_b	J_c
$^P P_2$	$^P Q_{12}$	J_a-1	J_a
$^Q Q_1$	$^Q P_{21}$	J_a	J_a-1
$^Q Q_2$	$^Q R_{12}$	J_a	J_a+1
$^R R_1$	$^R Q_{21}$	J_a+1	J_a
	$^O P_{12}$		J_a-1
$^P P_1$		J_a-1	
$^R R_2$		J_a+1	
	$^S R_{21}$		J_a+1

If we consider the (0-0) band of the $\tilde{A}$-$\tilde{X}$ system of NO, the known values are $Re = 1.56 \times 10^{-30}$ C m and $|\langle v_a | v_b \rangle|^2 = 0.167$. The $S_{\alpha\beta}^J$ values of NO are calculated according to [41,36,24] for the main and satellite lines.

We define the so-called Rabi frequency $\Omega_{\alpha\beta}$ of the $|\alpha\rangle \rightarrow |\beta\rangle$ transition as

$$\Omega_{\alpha\beta} = \frac{|\mu_{\alpha\beta}||E|}{hc}, \tag{55}$$

which becomes

$$\Omega_{\alpha\beta} = \frac{Re|\langle v_a | v_\beta \rangle|(S_{\alpha\beta}^J)^{1/2}|E|}{hc}. \tag{56}$$

We then define a vibronic Rabi frequency Ω_{vib} such as

$$\Omega_{\alpha\beta} = \Omega_{\text{vib}}(S_{\alpha\beta}^J)^{1/2}, \tag{57}$$

with

$$\Omega_{\text{vib}} = \frac{Re|\langle v_a | v_\beta \rangle||E|}{hc} \quad \text{cm}^{-1}. \tag{58}$$

This further decomposition consists in separating the rotational part $S_{\alpha\beta}^J$ of the transition moment in order to have a single vibronic Rabi frequency for each NO band. Hence, the electric field can be expressed as a function of Ω_{vib} according to the above NO data such as

$$|E| = \Omega_{\text{vib}} \times 6.3 \times 10^7 \quad \text{V/m}. \tag{59}$$

It is now equivalent to plotting the spectra as a function of Ω_{vib} or E. Therefore, in the following and for sake of simplicity, only Ω_{vib} is scaled on the X axis in the different figures. The collisional linewidths are detailed in the next section prior to undertaking some example of calculation.

C. Collisional data

The collisional parameters required in the model are defined in Eqs. (34). We shall make the following assumptions on the collisional rates

(1) $\Gamma_{ab}(k)$, $\Gamma_{ac}(k)$, and $\Gamma_{bc}(k)$ are not dependent on k;
(2) $\Gamma_{ab}(k) = \Gamma_{ac}(k) > \Gamma_{bc}(k)$;
(3) $\Gamma_{\alpha\beta}(k)$ is always larger than $\Gamma_\alpha(k)$ and $\Gamma_\beta(k)$, because of the dephasing contributions $\Gamma_{\alpha\beta}^\phi$ defined in Eq. (35);
(4) $\Gamma_b(k) = \Gamma_c(k)$; $\Gamma_{bc}(k) = \Gamma_{cb}(k)$; $\Theta_{ab}(k) = \Theta_{ac}(k)$; $\Theta_{bc}(k) = \Theta_{cb}(k)$.

Williams *et al.* have shown that population and reorientation relaxation rates are nearly equal for low J in OH [42]. It was shown that rotational level dependence of Γ_α is not observed in NO [43,44]. Therefore we assume, whatever J in NO, that

$$\Gamma_\alpha(k > 0) = 2\Gamma_\alpha(k = 0). \tag{60}$$

In order to find their numerical values, the rates appearing in Eqs. (34) are further expressed in terms of specific rates. Namely, relaxation rates are decomposed into

R_α^{RET}, Q_α, and A_α^{es} that label respectively the rotational energy transfer rate, the quenching rate and the Einstein coefficient for spontaneous emission from the $|\alpha\rangle$ level [45,46]. We also need to define $R_{\beta\alpha}^{\text{RET}}$, $Q_{\beta\alpha}$, and $A_{\beta\alpha}^{es}$ as state-to-state energy transfer rates from $|\alpha\rangle$ to $|\beta\rangle$.

$$\Gamma_a(k=0) = R_a^{\text{RET}},$$

$$\Gamma_b(k=0) = R_b^{\text{RET}} + Q_b + A_b^{es},$$

$$\Theta_{ab}(k=0) = Q_{ab} + A_{ab}(k=0),$$

$$\Theta_{ab}(k>0) = A_{ab}(k),$$

where $A_{ab}(k) = (-1)^{J_a + J_b + k + 1} A_b^{es} (2J_b + 1) \left\{ \begin{matrix} J_b & J_b & k \\ J_a & J_a & 1 \end{matrix} \right\}$ [47]

$$\Theta_{bc}(k=0) = R_{bc}^{\text{RET}},$$

$$\Theta_{bc}(k>0) = 0.$$

Let us note that Zeeman orientation is partially transferred by radiative processes between electronic levels whereas inelastic collisional transfer cannot preserve significantly orientation. The velocity changing collisions could preserve orientation but were disregarded in the present treatment [48].

Γ_{ab} is related to the homogeneous half width at half maximum (HWHM) of a dipolar transition between $|a\rangle$ and $|b\rangle$. The temperature and pressure dependence of Γ_{ab} is calculated for NO as [43,44]

$$\Gamma_{ab}(k) = \frac{1}{2} \left[0.79 \left(\frac{295}{T} \right)^{0.79} 0.3 + 0.585 \left(\frac{295}{T} \right)^{0.75} 0.7 \right] \times P \quad \text{cm}^{-1}$$

for a mixture of colliders of 30% H_2O and 70% N_2, where T is the temperature in Kelvin and P the pressure in atm.

In the $\tilde{X}^2\Pi$ and the $\tilde{A}^2\Sigma$ states, the rotational energy transfer data for NO were available mainly at room temperature [49–51]. We have extrapolated the tabulated value for the ground state in flame conditions [52] to our conditions for the excited state [53]. On the other hand, the quenching values are derived from Paul and co-workers' model for temperature-dependent quenching of NO $\tilde{A}^2\Sigma$ [54,55] and from high-temperature measurements [56]. The well-known spontaneous emission coefficient is taken from McDermid and Laudenslager [57]. Therefore, we will make a crude assumption that R^{RET}, Q, and A are not dependent on J and are the following for $v = 0$, $T = 2000$ K, and atmospheric pressure:

$$R_a^{\text{RET}} = R_b^{\text{RET}} = 2 \times 10^{-2} \quad \text{cm}^{-1},$$

$$Q_b = 4 \times 10^{-3} \quad \text{cm}^{-1},$$

$$A_b^{es} = 1.5 \times 10^{-4} \quad \text{cm}^{-1}.$$

In addition, the vibrational energy transfer is assumed negligible compared to the quenching and the rotational en-

TABLE II. NO data for collisional relaxation and Doppler broadening in cm^{-1}, in flame conditions ($T = 2000$ K, $P = 1$ bar), other related data are given through the interchange of b and c.

	$k=0$	$k>0$
$\Gamma_{ab}(k)$	7.49×10^{-2}	7.49×10^{-2}
$\Gamma_{bc}(k)$	4.90×10^{-2}	4.90×10^{-2}
$\Gamma_a(k)$	2.00×10^{-2}	4.00×10^{-2}
$\Gamma_b(k)$	2.45×10^{-2}	4.90×10^{-2}
$\Theta_{bc}(k)$	2.00×10^{-3}	0
Doppler (HWHM)	0.129	

For $Q_1P_{21}(5.5)$	$k=0$	$k=1$	$k=2$
$\Theta_{ab}(k)$	2.60×10^{-3}	1.50×10^{-4}	1.41×10^{-4}
$\Theta_{ac}(k)$	2.58×10^{-3}	1.38×10^{-4}	1.34×10^{-4}

ergy transfer processes [58]. Effects arising from velocity changing collisions are not treated here, since they were not observed for NO.

From these rates and the previous assumptions, the final numerical data introduced in the model are given in Table II for 2000 K and atmospheric pressure.

IV. SATURATION BEHAVIOR

Most of the calculations assume atmospheric pressure, a temperature of 2000 K, and a constant total number density N. In these conditions, Doppler broadening is equal to 0.129 cm^{-1} (HWHM). A doublet of line composed of $^QQ_1$ and $^QP_{21}$ will be called a Q_1P_{21} doublet for sake of simplicity. The full denomination is defined in Table I and is illustrated in Fig. 5. All other doublets are labeled in the same way in the following.

Saturation effects will be studied in most cases assuming equal field amplitudes of the exciting beams, that is $E_i = E$ with $i = 1,2,3$.

In Sec. IV A, we first compare the characteristics of the present model to previous results obtained in the weak-field limit, using perturbative theory, for isolated lines. A simplification of the input collisional parameters is done in this section in order to match the assumptions of the previous calculation [20] that disregards the multipole nature of relaxation and dephasing rates.

In Sec. IV B, the level $|c\rangle$ is again disregarded (Fig. 4) to study the saturation features of isolated lines that may be either main or satellite ones as listed in Table I. We consider here the complete collisional description of Sec. III C. The influence of the Zeeman structure and of unequal pump beam intensity on the saturation process will be described in detail.

In Sec. IV C, the rotational line coupling between $|b\rangle$ and $|c\rangle$ levels is fully accounted for, in order to observe the additional distortion of line profile and intensities resulting from this latter phenomenon. The effect of this line mixing resulting from strong-field excitation was not properly taken into account in previous works.
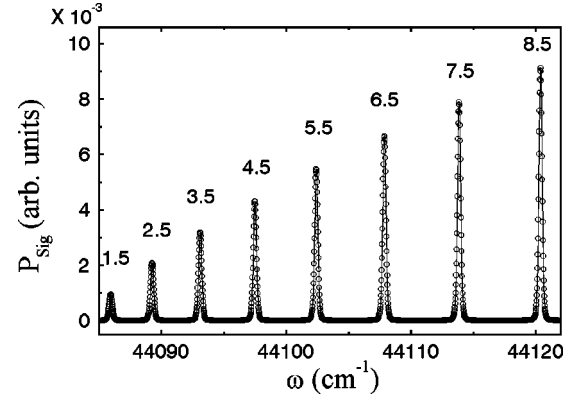

FIG. 6. Isolated $^QQ_2$-branch structure with (solid line) the perturbative model and ($\bigcirc$) the tensorial model with simplified assumptions: $\Gamma_a(k) = \Gamma_b(k) = \Gamma_{ab}(k), \forall k$, in the $yyyy$ configuration from $J=1.5$ to $J=8.5$ with $\Omega_{\text{vib}} = 10^{-3}$, $P=1$ bar, and $T = 2000$ K.

A. Low-field limit: comparison with the perturbative model for an isolated line

While the perturbative model has been successfully applied to the low-field limit in DFWM spectroscopy, our model concerns the whole range between no-saturation and high-saturation regimes. Let us first demonstrate that both models are equivalent in the low-field limit.

Some simplifications are done to compare the spectral line shapes obtained in the low-field regime. As in our previous treatments [19,20], we set $\Gamma_a(k) = \Gamma_b(k) = \Gamma_{ab}(k)$, whatever k. This assumption means that we neglect the pure dephasing rates and the multipole dependence of collisional linewidths. Moreover, the transfer rates $\Theta(k)$ and the spontaneous emission are set to zero.

In this way, the present model is compared to our previous perturbative treatment in Fig. 6 in which P_{Sig} is given by Eq. (53). The comparison is done for an isolated $^QQ_2$-branch in the $yyyy$ polarization and the two profiles are in quite good agreement with $\Omega_{\text{vib}} = 10^{-3}$.

Let us define a line amplitude ratio R by

$$\mathsf{R}_{yxyx} = \frac{P_{\text{Sig}}^{\max}(yxyx)}{P_{\text{Sig}}^{\max}(yyyy)} \quad \text{and} \quad \mathsf{R}_{yxxy} = \frac{P_{\text{Sig}}^{\max}(yxxy)}{P_{\text{Sig}}^{\max}(yyyy)}. \quad (61)$$

These ratios correspond to the ratio of P_{Sig} at line maximum in crossed-polarization configurations over $P_{\text{Sig}}^{\max}$ in the all-parallel case. They are plotted in Figs. 7(a) and (b) for P and Q lines, respectively. The analytical ratios of Bervas *et al.* [20] are plotted in Fig. 7, case A. The case B is calculated with our computed ratios and is in good agreement with case A. The line amplitude calculated from our model is therefore fully consistent with previous analytical description of DFWM signal intensity performed in the perturbative limit.

These line amplitude ratios depend only on the geometrical factors in case A and B [20,28]. The $R(J)$ line ratio is found equal to the ratio of $P(J+1)$ line and thus is not considered here. If the only transfer processes occurring between $|b\rangle$ and $|a\rangle$ are that induced by the laser, the geometri-
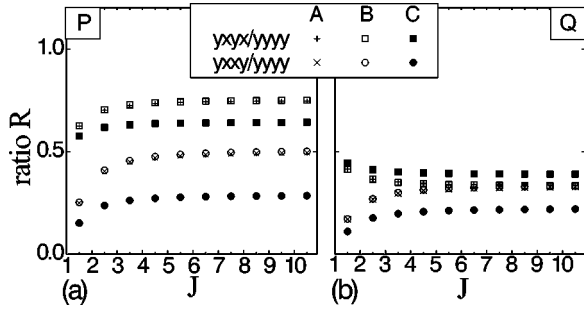
FIG. 7. Analytical and computed line-amplitude ratios of (a) P and (b) Q branches with $\Omega_{\mathrm{vib}}=10^{-3}$, $P=1$ bar, and $T=2000$ K. A: calculated with analytical formula of [20]; B: computed with tensorial model and simplified assumptions: $\Gamma_a(k)=\Gamma_b(k)=\Gamma_{ab}(k),\forall k$; C: computed with tensorial model and collisional assumptions of Table II.

cal factors involved in our expressions are the same for these two types of line.

In Fig. 7, the computed ratios obtained using the collisional data of Table II (case C) are also shown for comparison. The particular effect of the dephasing rate and k-dependence included in our complete relaxation-rates model tends to change the final R values. Since in cases A and B, disorienting collisions are neglected, the amplitude ratios R, which depend on geometrical factors, do not depend on any Γ_α values. In case C, we have introduced the disorienting collisions that are seen to strongly change the efficiency of signal generation, especially in crossed-polarization cases. The influence of anisotropic transfer is also playing a role but of minor importance (see Appendixes A and B). This tendency is of crucial importance in some cases even at low energy thresholds [25–27]. Finally, one advantage of the tensorial approach is to take properly into account the effect of disorientation through collisions, in the spectral line shapes.

B. Saturation of an isolated line

The properties of isolated lines (main or satellite) are studied here as a function of several parameters such as rotational quantum number, field strength, Zeeman multiplicity, and different relative amplitudes of the beams. Some of these effects were already studied in the past [12,24], but it is the first time to our knowledge that both polarization and saturation are studied thoroughly for the different NO lines listed in Table I. Let us note that the cases of OH and CH, although not detailed in the present paper, can be studied straightforwardly from our model. The data of Table II are used in all the following calculations and particularly the k-dependent linewidths including dephasing contributions.

1. Rabi broadening of rotational lines

The so-called Rabi frequency Ω_{ab} of the $|a\rangle\rightarrow|b\rangle$ transition interacting with the total electric field $\vec{\mathbf{E}}$ was introduced in Sec. III B.

More precisely, to quantify the saturation threshold of a rovibrational transition, a saturation parameter is commonly defined as [24,22]

TABLE III. Saturation thresholds S_{ab} and other parameters relatives to saturation of isolated $^PP_1(5.5)$, $^QQ_1(5.5)$, and $^RR_1(5.5)$ lines for homogeneous distribution of the beam amplitudes and polarization.

		$S_{ab}=1$	Dip appearance	
	$(S_{ab}^J)^{1/2}$	$\Omega_{\mathrm{vib}}^{\mathrm{sat}}$	Ω_{vib}	S_{ab}
$^PP_1(5.5)$	1.81	0.02	0.2	87
$^QQ_1(5.5)$	2.65	0.015	0.12	67
$^RR_1(5.5)$	1.92	0.02	0.2	97

$$S_{ab}=\frac{\Omega_{ab}^2}{\Gamma_a\Gamma_{ab}}. \tag{62}$$

From this expression, it is clear that the degree of saturation depends on the type of transition and on the collisional environment. We choose to define the saturation threshold by $S_{ab}=1$, which corresponds to $\Omega_{ab}^{\mathrm{sat}}=\Omega^{\mathrm{sat}}\sqrt{S_{ab}^J}=\sqrt{\Gamma_a\Gamma_{ab}}$ and

$$E_{\mathrm{sat}}=\frac{hc\sqrt{\Gamma_a\Gamma_{ab}}}{|\mu_{ab}|}. \tag{63}$$

Some values of Ω^{sat} are given in Table III for the $^PP_1$, $^QQ_1$, and $^RR_1$ lines of NO with $J=5.5$. For the $^QQ_1(5.5)$ isolated line, the line-broadening behavior of the line shape is illustrated in Fig. 8 with appearance of a dip between $\Omega_{\mathrm{vib}}=0.1$ and $\Omega_{\mathrm{vib}}=5$.

According to the previous definition of the threshold, saturation becomes visible on the spectra as soon as the Rabi frequency becomes larger than the relaxation rates.

2. Line intensity in various branches

The FDFWM polarization P_{Sig} is plotted at line maximum ($P_{\mathrm{Sig}}^{\mathrm{max}}$) and not at line center as done usually. The logarithmic plot of Fig. 9 exhibits a cubic field dependence below $\Omega_{\mathrm{vib}}=0.01$ [20], as predicted by the perturbative theory. The signal dependence versus Ω_{vib} is changing between
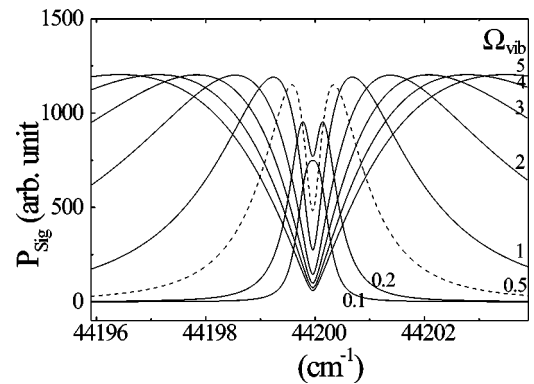

FIG. 8. Line-shape behavior of an isolated main $^QQ_1(5.5)$ line with $\Omega_{\mathrm{vib}}=0.1$ to 5 in the $yyyy$ configuration and with $P=1$ bar, $T=2000$ K, and collisional data of Table II; for that particular line, $\Omega^{\mathrm{sat}}=0.015$, $E_{\mathrm{sat}}=9.40\times10^5$ V/m, and $I_{\mathrm{sat}}=58$ kW/cm^2 at saturation threshold. However, the dip appears above $\Omega_{\mathrm{vib}}=0.12$ only, i.e., for $I>100I_{\mathrm{sat}}$.
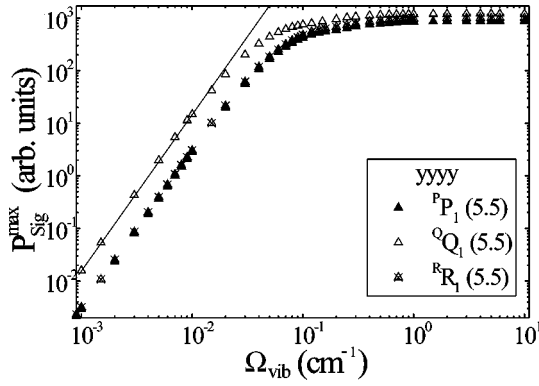
FIG. 9. Evolution of the signal at line maximum for isolated $^PP_1(5.5)$, $^QQ_1(5.5)$, and $^RR_1(5.5)$ lines in $yyyy$ configuration with $P=1$ bar, $T=2000$ K, and collisional data of Table II. As expected, the slope of all curves is 3 in logarithmic scale, below the saturation limit.

$\Omega_{vib}=0.01$ and $\Omega_{vib}=1$, around the Ω^{sat} value, already given in Table III, thus defining what we will call an intermediate range. Above $\Omega_{vib}=1$, the strong saturation condition gives a plateau.

The $^PP_1$, $^QQ_1$, and $^RR_1$ line amplitudes are presented in Figs. 10(a–c) as a function of Ω_{vib} and for the $yyyy$, $yxyx$,

and $yxxy$ configurations. In Fig. 10(b), the $^RR_1$ line becomes stronger than the $^QQ_1$ one, beyond $\Omega_{vib}=0.3$, indicating that, in the $yxyx$ polarization, saturation has a more pronounced effect on the $^QQ_1$-branch relative to $^RR_1$ one. $^QQ_1$ line always dominates $^PP_1$ line in all cases. In the $yxxy$ configuration [Fig. 10(c)], $^RR_1$ is always smaller than $^QQ_1$ whatever Ω_{vib}.

The efficiency η is defined as

$$\eta = \frac{I_{Sig}}{\sum_i I_i} \quad \text{where } I_i \propto |E_i|^2. \tag{64}$$

As shown in Figs. 10(d–f), the efficiency at line maximum (η_{max}) grows quadratically to reach a maximum value lying around $\Omega_{vib}=0.1$ for all lines. Therefore, the intermediate range of saturation is the laser energy range providing optimum sensitivity for concentration measurements, as demonstrated by former works [12,24,59]. The maximum efficiency is always higher for the Q-branch, than for the P and R ones, and its absolute value decreases from $yyyy$ to $yxyx$ and $yxxy$ configurations. Nevertheless, as we will see later on, crossed-polarization cases could become advantageous since they offer the possibility to reduce the scattered light on the signal path.
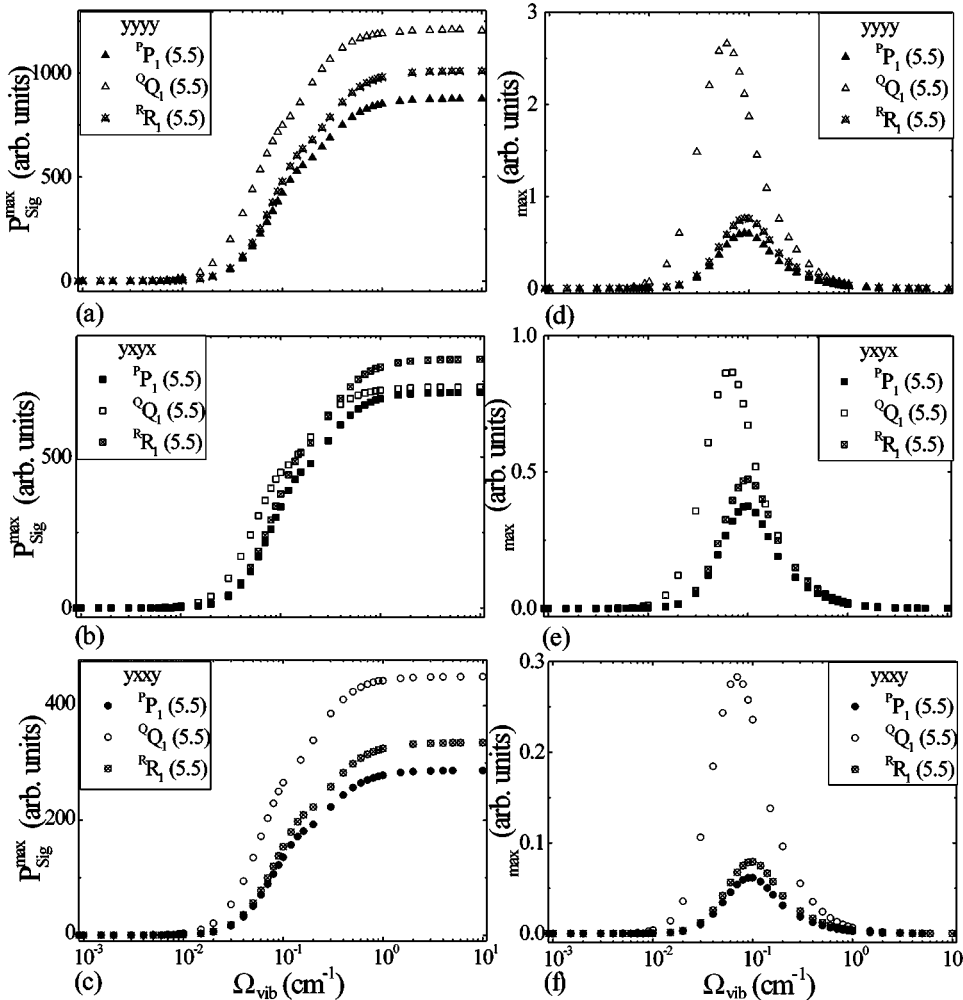

FIG. 10. Evolution (a,b,c) of the signal at line maximum and (d,e,f) of the efficiency η at line maximum as a function of Ω_{vib} for isolated $^PP_1(5.5)$, $^QQ_1(5.5)$, and $^RR_1(5.5)$ lines in different polarization configurations with $P=1$ bar, $T=2000$ K, and collisional data of Table II.
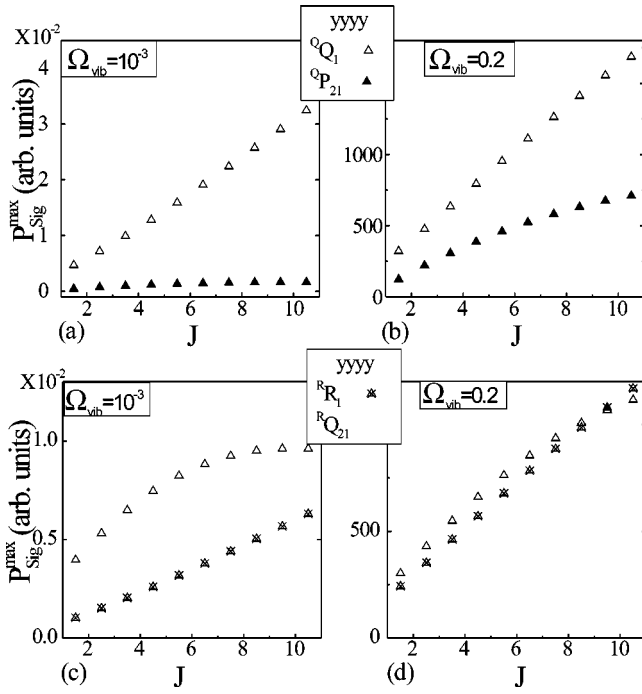
FIG. 11. Evolution of the signal at line maximum as a function of J for $yyyy$ polarization configuration for $\Omega_{vib} = 10^{-3}$ and $\Omega_{vib} = 0.2$; upper graph corresponds to the main line $^QQ_1$ and its satellite $^QP_{21}$ and lower graph to the main line $^RR_1$ and its satellite $^RQ_{21}$ in the same conditions as Fig. 10.

The $^QQ_1$, $^QP_{21}$, $^RR_1$, and $^RQ_{21}$ branches are shown in Figs. 11 and 12 for the all-parallel and crossed-polarized cases, respectively. The behavior of main and satellite line intensity is calculated as a function of J for $\Omega_{vib} = 10^{-3}$ and 0.2. In the low-field limit, these line amplitudes have already
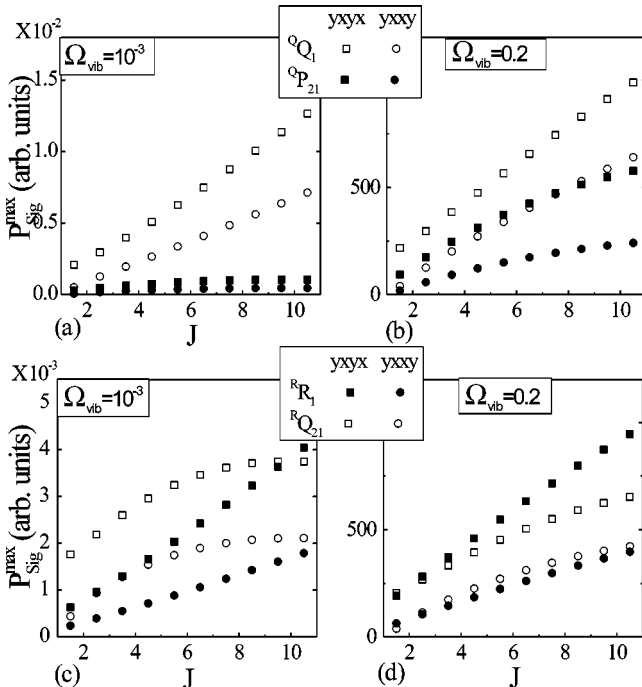
FIG. 12. Same figure as Fig. 11 for $yxyx$ and $yxxy$ polarization.
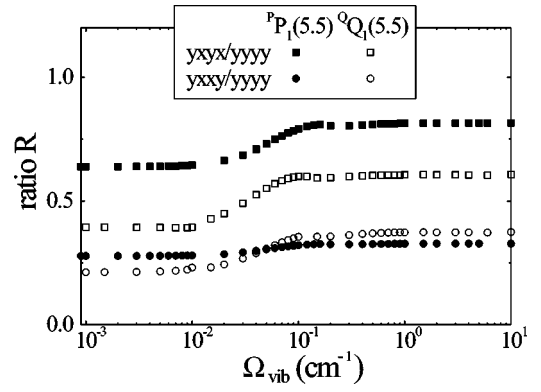
FIG. 13. Evolution of ratios R at line maximum as a function of Ω_{vib} for isolated $^PP_1(5.5)$ and for $^QQ_1(5.5)$ lines and the same conditions as Fig. 10.

been used to calculate the ratios R of Fig. 7(c). We can notice that at low intensity, the Q lines always give the largest signals as well when it is a main line ($^QQ_1$-$^QP_{21}$) as when it is a satellite line ($^RR_1$-$^RQ_{21}$). In this case, a crossing appears for $J = 10.5$ in the $yxyx$ and $yxxy$ configurations and should appear above $J = 11.5$ in the $yyyy$ case. At higher saturation ($\Omega_{vib} = 0.2$), the difference between the main and the satellite line is reduced. For the $^RR_1$ and $^RQ_{21}$ lines, $^RR_1$ line passes over its satellite line $^RQ_{21}$ at $J = 2.5$ in the $yxyx$ case. The prediction of these branches' behaviors will be particularly useful to interpret the experimental spectra of NO [V. Krüger *et al.*, paper II].

As previously demonstrated in Sec. IV A [20,26–28], all the information regarding the experimental polarization geometry is included in the geometrical factors of the resonant four-wave-mixing response. The ratios R of Eq. (62) that directly reflect these geometrical factors are plotted as a function of Ω_{vib} in Fig. 13 for $^PP_1(5.5)$ and $^QQ_1(5.5)$ lines. As expected from the perturbation theory [20], R ratios do not depend on laser intensity as far as the low-field approximation is valid ($\Omega_{vib} < 0.01$). In the intermediate range ($0.01 < \Omega_{vib} < 0.1$), the saturation occurs differently for the different polarization configurations and all ratios vary. It means that although each Zeeman transition has its own transition probability that is at the origin of the geometrical factors in the low-field limit [24–27], the saturation tends to erase this difference above a certain threshold.

A remarkable feature is the occurrence of a new plateau of R values in the high-saturation range. New factors can be derived from the high-field plateau's value. The line intensity derivation in the saturation limit could be greatly simplified using these factors. In particular, it may be quite interesting to study the evolution of that plateau as a function of the Γ_α values and more particularly of the amplitude of the disorienting collisions. Let us notice also that the crossed-polarization arrangements are more advantageous in the high-field limit since R values become larger as already mentioned in [21].

Finally, the utility of our model is demonstrated when exact calculation of the intensity is required, especially in the intermediate range. In this case, analytical expressions previously published [11,60] are not anymore appropriate.
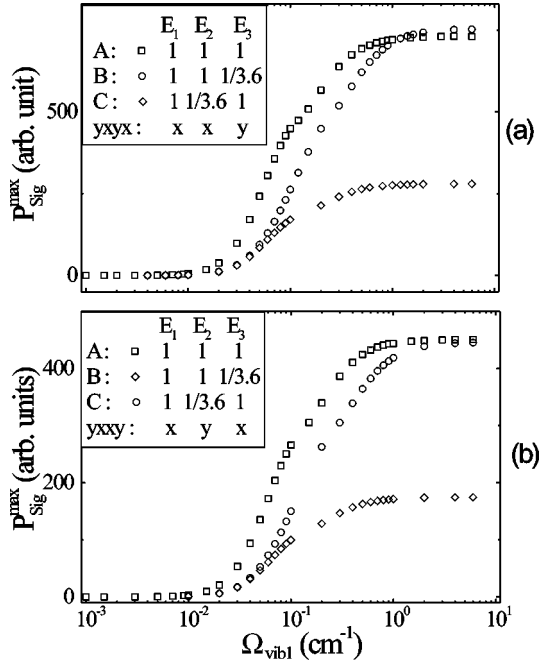
FIG. 15. Line-shape behavior vs ground rotational level J for an isolated main $^{Q}Q_1$ line from $J=1.5$ to $J=7.5$ with $\Omega_{\text{vib}}=0.5$ and the same conditions as Fig. 10; we use a fixed value $S_{ab}^{J}=S_{ab}^{J=5,5}\forall J$ in this particular case. Dashed curve refers to $J=5.5$.

ing. Therefore, the $yxxy$ configuration, with attenuation of the y-polarized probe beam 2, is preferred since only coherence gratings are generated.

4. Influence of Zeeman multiplicity

The saturation of FDFWM signal intensity is the result of two competing effects: the line strength of the multiplicity expressed by the factor S_{ab}^{J} [Eq. (55)] and the individual amplitude of each Zeeman component, the average value of which decreases like $\sqrt{2J+1}$ when the number of components increases (as it can be seen from the value of 3-j coefficients).

The effect of the M-level degeneracy is illustrated in Fig. 15 as a function of J, for $\Omega_{\text{vib}}=0.5$. In order to observe the effect of the change of 3-j coefficients with J separately, we choose to keep S_{ab}^{J} fixed in the calculation of the line profiles [Eq. (55)]. In this case (Fig. 15), the line profile becomes narrower when J increases, indicating that saturation is attenuated by the increasing number of Zeeman sublevels.

In Fig. 16, the signal intensity is normalized at line maximum for $J=1.5$ and $J=11.5$. In Fig. 16(a), exact calculation of the line profile shows that the saturation is almost the same whatever J for the main $^{Q}Q_1$ lines. The change of S_{ab}^{J} is roughly following a $(2J+1)^n$ law with a larger n value for main than for satellite lines [20]. Figure 16(b) shows that

FIG. 14. Evolution of $P_{\text{Sig}}^{\text{max}}$ as a function of Ω_{vib1} for isolated $^{Q}Q_1(5.5)$ line: in the $yxyx$ configuration (a) and in the $yxxy$ configuration (b); A: $E_1=E_2=E_3$; B: $E_2=E_1,E_3=E_1/3.6$; C: $E_2=E_1/3.6,E_3=E_1$. Ω_{vib1} is the vibronic Rabi frequency of beam 1.

3. Unequal beam intensity

We have performed numerical calculations of the signal amplitude P_{Sig} for several distributions of the incident laser energy over the three input beams. To be consistent with our experimental conditions, we assume that two beams have the same field amplitude whereas the y-polarized beam is attenuated by a factor of 3.6, this value corresponding to the laser attenuation used in [V. Krüger *et al.*, paper II].

Figure 14 illustrates the evolution of the signal amplitude at line maximum of the $^{Q}Q_1(5.5)$ isolated line in different polarization arrangements and energy distributions. The distribution is uniform in the A case ($E_1=E_2=E_3$). The DFWM signal is always more efficient in this case, in good agreement with the study of Ai and Knize [4] in phase conjugate geometry.

The pump beam 3 has been attenuated in case B and the probe beam 2 in case C. In both polarization configurations, the signal is only slightly reduced in the intermediate saturation regime, when the attenuated incoming beam is the one that is y polarized, like the signal {case B for $yxyx$ [Fig. 14(a)] and case C for $yxxy$ [Fig. 14(b)]}. On the opposite, attenuation of a x-polarized beam strongly reduces the signal. Let us note that Fig. 14 is plotted as a function of the vibronic Rabi frequency of beam 1.

This result is extremely interesting since, for obvious problems of noise rejection, the best experimental situation consists in attenuating the exciting beam that is polarized like the signal beam.

However, as we will see in the experimental article [V. Krüger *et al.*, paper II], the intensity cannot be increased up to the high-saturation regime, in the $yxyx$ case, because the population grating induces a spurious parasitic thermal grat-
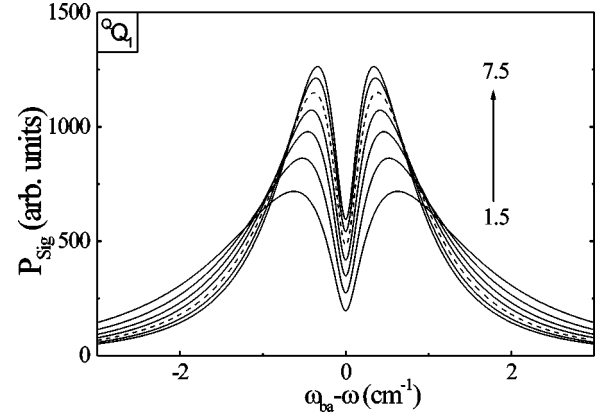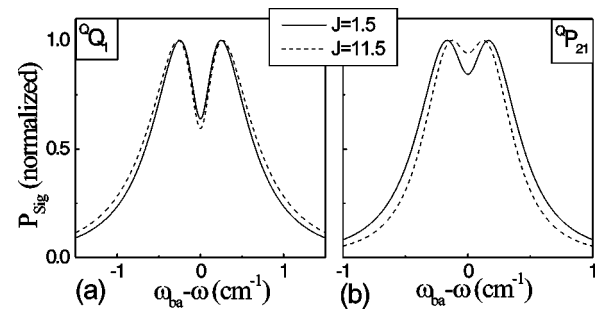

FIG. 16. Normalized line-shape behavior vs J for main $^{Q}Q_1$ (a) and satellite $^{Q}P_{21}$ (b) lines for $J=1.5$ and $J=11.5$ with $\Omega_{\text{vib}}=0.3$ and the same conditions as Fig. 10.
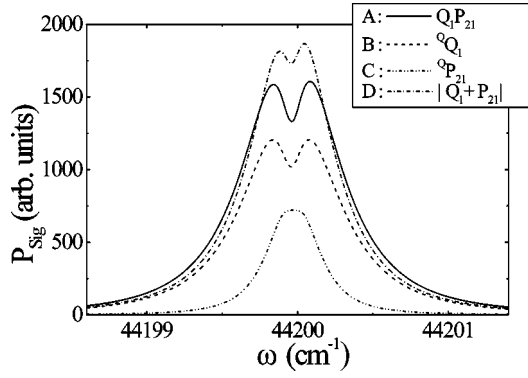
FIG. 17. Line-shape behavior with $\Omega_{\text{vib}}=0.2$, $\omega_{bc}=0.015$ cm^{-1} and the same conditions as Fig. 10, for the $Q_1P_{21}(5.5)$ doublet (A), its singlet components $^QQ_1(5.5)$ (B) and $^QP_{21}(5.5)$ (C) and the complex sum of these two components (D).

saturation of satellite $^QP_{21}$ lines decreases when J increases, since S_{ab}^J increases much less than the 3-j coefficients decrease. Nevertheless, the effect of rotational degeneracy may be further complicated when main and satellite components are coupled by the strong fields as described in the next section.

C. Saturation including rotational line coupling

Let us remember that a doublet transition involves a main line $|a\rangle \rightarrow |b\rangle$ and a satellite line $|a\rangle \rightarrow |c\rangle$. The final behavior of the doublet profile depends on the relative line strength of its single components and on the splitting between them ω_{bc}.

In this section, all calculations are performed assuming a coupled three-J level scheme (Fig. 4) and the collisional assumption of Table II at 2000 K. The line intensities are derived from the definition (54) and simulations will be presented in order to isolate the line mixing effects that couple main and satellite components of NO doublets under strong-field excitation.

Peculiar effects of line coupling between main and satellite components will be recognized by comparison with line profiles obtained by simply adding the independently calculated complex amplitudes of the nonlinear polarization of nearby transitions.

The Q_1P_{21} doublet is plotted in Fig. 17 in the $yyyy$ polarization. The profiles of the two components and of their sum are also shown. In the intermediate saturation regime ($\Omega_{\text{vib}}=0.2$), the sum leads to a stronger intensity than the coupled doublet profile that exhibits a deeper hole. The coupling between the two components reinforces the saturation process, since the population of the common $|a\rangle$ level is shared by both transitions. In four-wave-mixing spectroscopy, many authors use the simple sum of amplitudes to describe line interferences. This summation is proved to be incorrect in doublet configurations such as that of NO.

1. Asymmetry and line interferences

A typical doublet splitting in NO is 0.015 cm^{-1} for $Q_1P_{21}(5.5)$ doublet and 0.017 cm^{-1} for $R_1Q_{21}(5.5)$ dou-
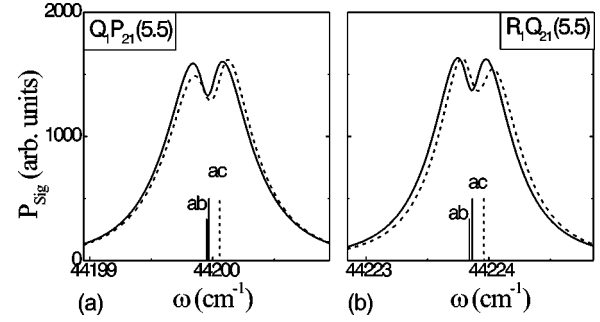
blet. The line strength factors S_{ab}^J and S_{ac}^J are similar for the components of the $R_1Q_{21}(5.5)$ doublet whereas the main component of the $Q_1P_{21}(5.5)$ doublet is almost two times stronger than the satellite one, thus leading to different features [24]. We choose to plot these doublets in the $yyyy$ polarization and by setting arbitrarily $\omega_{bc}=0.01$ cm^{-1} and 0.1 cm^{-1} in Fig. 18. Medium saturation is assumed in this case with $\Omega_{\text{vib}}=0.2$. The splitting ω_{bc} has a definite influence on the final line shape behavior. A large ω_{bc} (0.1 cm^{-1}) results in an asymmetric profile as it is expected since lines are almost resolved ($\Gamma_{ab}=\Gamma_{ac}=0.0749$ cm^{-1}). As depicted in Fig. 18, the $R_1Q_{21}(5.5)$ and $Q_1P_{21}(5.5)$ doublets exhibit opposite asymmetry since their μ_{ab}/μ_{ac} values are different. The highest peak seems to be located on the side corresponding to the weakest component. By separating real and imaginary parts in the calculation of the complex polarization, we have seen that the asymmetry is mainly originating from the contributions of the dispersive parts to the line profile.

Similarly, the influence of the polarization on the asymmetry is shown in Fig. 19 with $\omega_{bc}=0.015$ cm^{-1}. One can notice the asymmetry is inverted comparing the $R_1Q_{21}(5.5)$ and $Q_1P_{21}(5.5)$ doublet line shapes for any polarization configuration. The asymmetry is stronger for the crossed-polarization cases than for the intense $yyyy$ one. Opposite asymmetry is observed for the $yxyx$ and $yxxy$ cases. While doing the calculation, we have seen that it is due to the
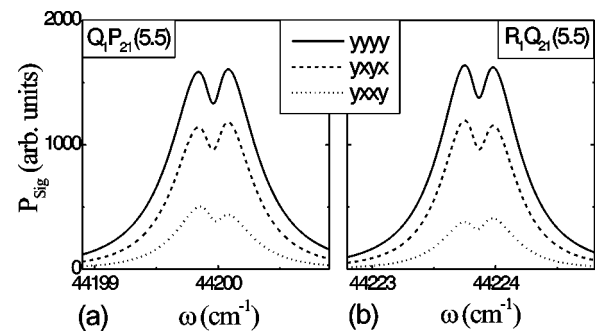

FIG. 18. Line-shape behavior for $Q_1P_{21}(5.5)$ (a) and $R_1Q_{21}(5.5)$ (b) doublets with $\Omega_{\text{vib}}=0.2$, $\omega_{bc}=0.01$ cm^{-1} (solid line) and $\omega_{bc}=0.1$ cm^{-1} (dashed line).

FIG. 19. Line-shape behavior for $Q_1P_{21}(5.5)$ (a) and $R_1Q_{21}(5.5)$ (b) doublets with $\Omega_{\text{vib}}=0.2$ and $\omega_{bc}=0.015$ cm^{-1} in the different polarization configurations and the same conditions as Fig. 10.

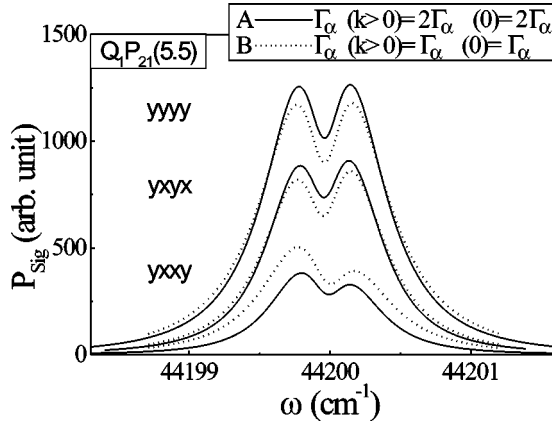FIG. 20. Line-shape behavior for $Q_1P_{21}(5.5)$ doublet with $\Omega_{vib}=0.2$ in the $yyyy$, $yxyx$, and $yxxy$ configuration: comparison of different collisional situations with $\Gamma_a=2.00\times10^{-2}$ cm^{-1}, $\Gamma_b=2.45\times10^{-2}$ cm^{-1} and other parameters from Table II.

contribution of the dispersive part of the line profile that is larger in the $yxxy$ case. The peculiar asymmetry of the $yxxy$ line shape has been already observed in the experiment of Kumar *et al.* [61] in CH.

One can conclude that ω_{bc}, μ_{ab}/μ_{ac}, and the polarization arrangement have a noticeable influence on the coupling effect when the calculations are performed in the intermediate range of saturation.

2. Contributions of orientational relaxation rates

The pure disorienting rates may be quite different depending on the collision partners. Let us notice that in some cases, as for helium colliders for example, this rate may increase significantly [42].

To evaluate the contributions of disorienting collisions, the $Q_1P_{21}(5.5)$ doublet profile is plotted in Fig. 20, assum-

ing different disorienting rates, $[\Gamma_\alpha(k>0)]$. In all cases, the optical dephasing rate $\Gamma_{a\beta}$ is kept constant. In case A, $\Gamma_\alpha(k>0)$ is set as twice the population rate of NO like in all previous calculations. In case B, disorienting contributions are canceled by setting $\Gamma_\alpha(k>0)=\Gamma_\alpha(k=0)$. With $yyyy$ and $yxyx$ configurations, the elimination of disorienting collisions results in a small increase of saturation with reduction of the amplitude and broadening of the line shape. It indicates that Zeeman coherences participate moderately in the saturation of optical transitions. For the $yxxy$ configuration, there is a relatively strong increase of the signal when there is no disorientation; this behavior highlights the importance of Zeeman coherences in the polarization gratings formation.

3. Line intensity versus E and J

The FDFWM signal polarization and the efficiency at line maximum are plotted in Fig. 21 as a function of Ω_{vib} for the $Q_1P_{21}(5.5)$ and $R_1Q_{21}(5.5)$ doublets. In the $yxyx$ case [Fig. 21(a)], the intensities of $Q_1P_{21}(5.5)$ and $R_1Q_{21}(5.5)$ doublets are practically identical although P, Q, and R isolated lines had different amplitudes in Fig. 10(b). In the $yxxy$ case [Fig. 21(c)], the saturated signal is different for the two doublets. However, the tendency is the same in both cases, i.e., the ratio of line amplitude Q_1/R_1 is smaller if line coupling is taken into account.

The effect of line mixing is further detailed in Fig. 22 as a function of J for $\Omega_{vib}=0.2$. The two components of each doublet are shown in Figs. 22(a) and (b), they are summed in Fig. 22(c) and coupled in Fig. 22(d). The behavior of the doublets amplitudes versus J is confirming that Q_1P_{21}/R_1Q_{21} ratio provides a good marker of this coupling effect as it will be observed experimentally [V. Krüger *et al.*, paper II].

In Fig. 23, the doublet amplitude P_{Sig} is calculated as a function of Ω_{vib} at different distance δ from line center, i.e.,
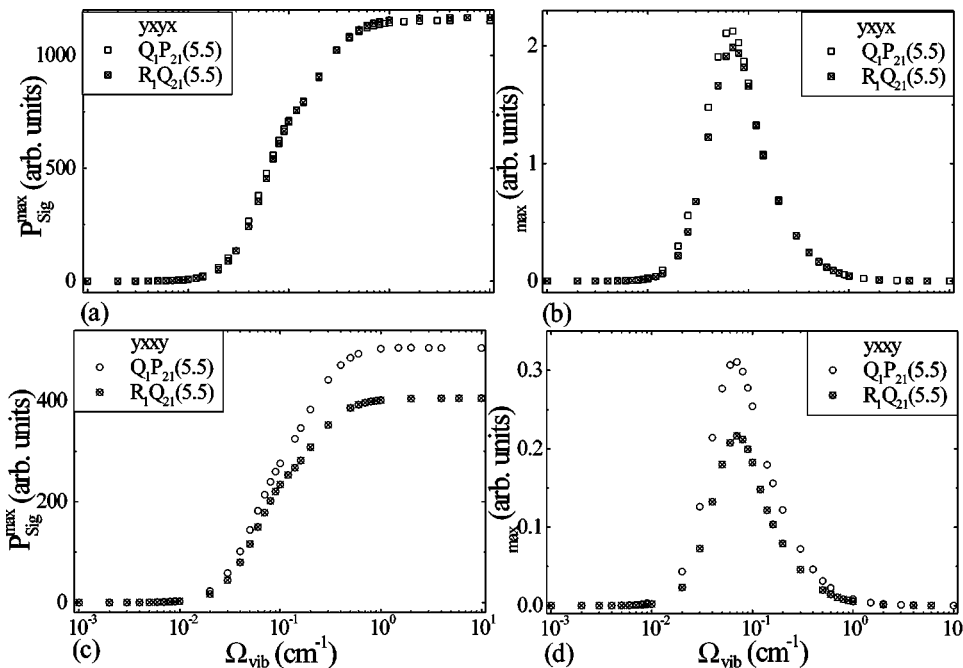

FIG. 21. Evolution of the signal at line maximum (a,c) and of the efficiency η at line maximum (b,d) as a function of Ω_{vib} for $Q_1P_{21}(5.5)$ and $R_1Q_{21}(5.5)$ doublets in $yxyx$ and $yxxy$ polarization configurations and the same conditions as Fig. 10.
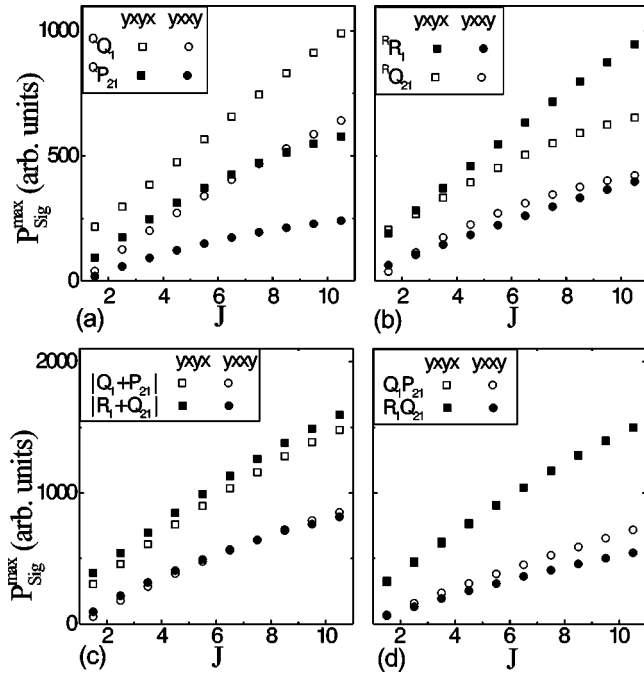
FIG. 22. Evolution of the signal at line maximum as a function of J for $yxyx$ and $yxxy$ polarization configurations with $\Omega_{vib} = 0.2$ in the same conditions as Fig. 10. a: main $^QQ_1$ and its satellite $^QP_{21}$; b: main $^RR_1$ and its satellite $^RQ_{21}$; c: the complex sum of the components amplitudes of the Q_1P_{21} and R_1Q_{21} doublet; d: Q_1P_{21} and R_1Q_{21} doublets.

FIG. 23. Evolution of the signal at different detuning frequencies δ as a function of Ω_{vib} for $Q_1P_{21}(5.5)$ doublet and $yyyy$ case in the same conditions as Fig. 10.

with $\delta = 0$, $2\Gamma_{ab}$, and $5\Gamma_{ab}$. If $\delta = 0$, the optimum efficiency of the process is obtained for $\Omega_{vib} = 0.15$. Larger input-laser intensities are required to reach this optimum condition if the laser frequency is detuned: $\Omega_{vib} = 0.25$ if $\delta = 2\Gamma_{ab}$ and $\Omega_{vib} = 0.5$ if $\delta = 5\Gamma_{ab}$. However, the amplitude of the maximum is larger in these cases than with $\delta = 0$. These results are consistent with the calculation of Ai and Knize in the phase conjugate geometry [4].

V. CONCLUSION

Our purpose was to properly take into account the saturation effects in forward DFWM for unresolved doublet lines, with specific polarization of the incoming beams, with the Zeeman structure and the disorienting collisions. A model based on irreducible tensor formalism is proposed to solve the density matrix equations. The system is solved in the steady-state approximation using a numerical matrix inversion. The signal amplitudes and line shapes are calculated in detail to study separately the effect of these different assumptions. The $2J+1$ Zeeman degeneracy has a small effect on the saturated spectral profiles of the main lines, which are almost independent on J, but has a much stronger influence on satellite lines.

The influence of the disorienting collisions is seen to distort the spectral line shapes and to change significantly the line intensity. The peculiar effect of disorientation has been evide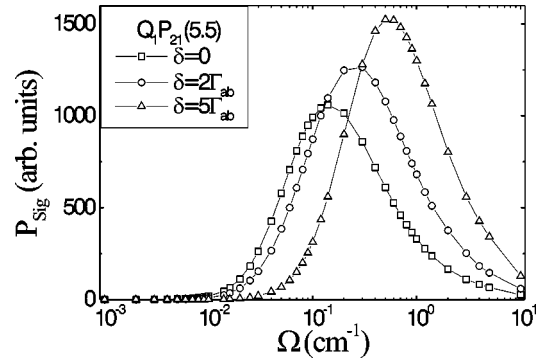nced in saturating conditions and this effect is large especially when pure coherence gratings are involved. To our knowledge, it is the first time that such effects are correctly simulated in the strong-field regime.

The rotational line coupling results in a stronger saturation of NO doublets and this effect is represented correctly through our calculation. Moreover, a line asymmetry is observed especially in crossed-polarization cases. The asymmetry may be reversed according to the polarization pattern. This effect is closely correlated to the strength of the transition moment and to the spacing between main and satellite transitions.

The intermediate domain of saturation is emphasized: it has been definitely proved as the most appropriate to provide optimal sensitivity in forward DFWM. In this regime, our treatment is necessary to allow quantitative measurements. The spatial profile of the laser may be incorporated in the calculation if necessary. Through this paper, we have discussed the saturation behavior of FDFWM. However, the model presented here involves analytical expressions that can be modified to represent other excitation schemes such as two-color resonant four-wave mixing, provided that each transition interact resonantly with only one laser frequency, allowing the rotating-wave approximation. Finally, for spectroscopic applications, the multipole nature of our treatment could be exploited to take into account the initial anisotropy existing in the molecular media although it would greatly increase the number of coupled equations [25–27]. In paper II, experimental measurements will be interpreted through the correct calculation of DFWM intensity whatever field strength, polarization, and line multiplicity.

APPENDIX A: DETAILED EXPRESSION OF THE EQUATION SET

In this appendix, we present the final expression of the density matrix equation reduced for the $_{ab}\rho_Q^k$ and $_{ac}\rho_Q^k$ components. These equations are solved numerically to calculate the $_{ab}\rho_Q^1$ and $_{ac}\rho_Q^1$ components required to obtain the expression of the DFWM signal polarization. In what follows, we rely on the definitions of symbols already introduced.

$$
[\omega - \omega_{ab} - i\Gamma_{ab}(k)]_{ab}\rho_Q^k = \frac{1}{4\hbar^2} \sum_{k' \neq 0,k''} \left\{ iB_{ab} \sum_{q,q',Q''} \mu_{ab}^2 E_q E_{-q'} [G_{1\,ab}\rho_{Q''}^{k''} - G_{2\,ab}\rho_{Q''}^{k''*}] + i(-1)^{J_b - J_c} C_{ab} \right.
$$

$$
\times \sum_{q,q',Q''} \mu_{ab}\mu_{ac} E_q E_{-q'} [G_{1\,ac}\rho_{Q''}^{k''} - G_{2\,ac}\rho_{Q''}^{k''*}] \Bigg\}
$$

$$
+ \frac{1}{4\hbar^2} \sum_{k',k''} \frac{\omega_{cb} + i\Gamma_{cb}(k')}{\omega_{cb}^2 + \Gamma_{cb}^2(k')} \left\{ R_{1ab} \sum_{q,q',Q''} G_1 \mu_{ac}^2 E_q E_{-q'\,ab}\rho_{Q''}^{k''} \right.
$$

$$
\left. - R_{2ab} \sum_{q,q',Q''} G_2 \mu_{ab}\mu_{ac} E_q E_{-q'\,ac}\rho_{Q''}^{k''*} \right\} + \delta_{k,1} \frac{1}{2\hbar^2\sqrt{3}} \left\{ \mathrm{Im}\left(\sum_{q'} A_b \mu_{ab}^2 E_Q E_{q'\,ab}\rho_{q'}^1 \right) \right.
$$

$$
\left. + \mathrm{Im}\left(\sum_{q'} A_{bc} \mu_{ab}\mu_{ac} E_Q E_{q'\,ac}\rho_{q'}^1 \right) \right\} + \delta_{k,1} \frac{E_Q}{2\hbar^2\sqrt{3}} \mu_{ab} \left\{ \frac{\rho_b^{(o)}}{\sqrt{2J_b + 1}} - \frac{\rho_a^{(o)}}{\sqrt{2J_a + 1}} \right\}
\tag{A1}
$$

with

$$
B_{ab} = (2k'+1)\sqrt{(2k+1)(2k''+1)} \left[\frac{1}{\Gamma_b(k')} \begin{Bmatrix} k'' & 1 & k' \\ J_b & J_b & J_a \end{Bmatrix} \begin{Bmatrix} k & 1 & k' \\ J_b & J_b & J_a \end{Bmatrix} \right.
$$

$$
\left. + \frac{(-1)^{k+k'}}{\Gamma_a(k')} \begin{Bmatrix} k' & 1 & k \\ J_b & J_a & J_a \end{Bmatrix} \left((-1)^{k'+k''} \begin{Bmatrix} k'' & 1 & k' \\ J_a & J_a & J_b \end{Bmatrix} + \frac{\Theta_{ab}(k')}{\Gamma_b(k')} \begin{Bmatrix} k'' & 1 & k' \\ J_b & J_b & J_a \end{Bmatrix} \right) \right],
\tag{A2}
$$

$$
C_{ab} = (2k'+1)\sqrt{(2k+1)(2k''+1)} \frac{(-1)^{k+k'}}{\Gamma_a(k')} \begin{Bmatrix} k' & 1 & k \\ J_b & J_a & J_a \end{Bmatrix} \left((-1)^{k'+k''} \begin{Bmatrix} k'' & 1 & k' \\ J_a & J_a & J_c \end{Bmatrix} + \frac{\Theta_{ac}(k')}{\Gamma_c(k')} \begin{Bmatrix} k'' & 1 & k' \\ J_c & J_c & J_a \end{Bmatrix} \right),
\tag{A3}
$$

$$
R_{1ab} = (2k'+1)\sqrt{(2k+1)(2k''+1)} \begin{Bmatrix} k'' & 1 & k' \\ J_c & J_b & J_a \end{Bmatrix} \begin{Bmatrix} k' & 1 & k \\ J_a & J_b & J_c \end{Bmatrix},
\tag{A4}
$$

$$
R_{2ab} = (2k'+1)\sqrt{(2k+1)(2k''+1)} \begin{Bmatrix} k'' & 1 & k' \\ J_b & J_c & J_a \end{Bmatrix} \begin{Bmatrix} k' & 1 & k \\ J_a & J_b & J_c \end{Bmatrix},
\tag{A5}
$$

$$
G_1 = \sum_{Q'} (-1)^{Q+Q''} \begin{pmatrix} k'' & 1 & k' \\ Q'' & q' & -Q' \end{pmatrix} \begin{pmatrix} k' & 1 & k \\ Q' & q & -Q \end{pmatrix},
\tag{A6}
$$

$$
G_2 = \sum_{Q'} (-1)^{Q+q'} \begin{pmatrix} k'' & 1 & k' \\ Q'' & q' & Q' \end{pmatrix} \begin{pmatrix} k' & 1 & k \\ Q' & q & -Q \end{pmatrix},
\tag{A7}
$$

$$
A_b = \frac{1}{\sqrt{3}} \left[\frac{1}{(2J_a+1)(2J_b+1)} \frac{\Gamma_c(0)\Theta_{ab}(0) + \Theta_{bc}(0)\Theta_{ac}(0)}{\Gamma_a(0)[\Gamma_b(0)\Gamma_c(0) - \Theta_{bc}^2(0)]} - \frac{1}{(2J_a+1)^2\Gamma_a(0)} - \frac{\Gamma_c(0)}{(2J_b+1)^2[\Gamma_b(0)\Gamma_c(0) - \Theta_{bc}^2(0)]} \right],
\tag{A8}
$$

$$A_{bc} = \frac{1}{\sqrt{3}} \left[\frac{1}{(2J_a+1)(2J_c+1)} \frac{\Gamma_b(0)\Theta_{ac}(0)+\Theta_{bc}(0)\Theta_{ab}(0)}{\Gamma_a(0)[\Gamma_b(0)\Gamma_c(0)-\Theta_{bc}^2(0)]} - \frac{1}{(2J_a+1)^2\Gamma_a(0)} \right.$$

$$\left. - \frac{\Theta_{bc}(0)}{(2J_b+1)(2J_c+1)[\Gamma_b(0)\Gamma_c(0)-\Theta_{bc}^2(0)]} \right]. \tag{A9}$$

The second equation for $_{ac}\rho_Q^k$ is obtained through the interchange of the index b and c. The notation $\text{Im}(\cdots)$ symbolizes the imaginary part of a complex quantity.

APPENDIX B: GENERAL EXPRESSION OF THE INTEGRAL OVER SPATIAL COORDINATES

In this appendix, we demonstrate the rigorous expression of the diffracted beam for any shape of the incoming beam and of the active volume. Through the knowledge of the incoming beams, it is possible to express $\mathcal{E}(\vec{r})$ in any point and to calculate $\mathcal{P}(\vec{r})$ according to Eq. (43). We use the spatial Fourier decomposition of $\mathcal{E}$ and $\mathcal{P}$

$$\mathcal{E}(\vec{r}) = \int \mathcal{E}(\vec{k})e^{i\vec{k}\cdot\vec{r}}d^3\vec{k}, \quad \mathcal{P}(\vec{r}) = \int \mathcal{P}(\vec{k})e^{i\vec{k}\cdot\vec{r}}d^3\vec{k}, \tag{B1}$$

$$\mathcal{E}(\vec{k}) = \frac{1}{(2\pi)^3} \int \mathcal{E}(\vec{r})e^{-i\vec{k}\cdot\vec{r}}d^3\vec{r},$$

$$\mathcal{P}(\vec{k}) = \frac{1}{(2\pi)^3} \int \mathcal{P}(\vec{r})e^{-i\vec{k}\cdot\vec{r}}d^3\vec{r}. \tag{B2}$$

The wave equation Eq. (45) leads to

$$(k^2-k_n^2)\mathcal{E}(\vec{k}) = \frac{k_n^2}{\varepsilon}\mathcal{P}(\vec{k}) \quad \text{with} \quad k_n = \frac{n\omega}{c}. \tag{B3}$$

We have assumed that the index of refraction is n everywhere for the final energy of the diffracted beam. As far as we measure the total intensity of the diffracted beam, this assumption has no importance.

The Fourier transform of $\mathcal{P}(\vec{k})$ is introduced in Eq. (B3) to give

$$\mathcal{E}(\vec{k}) = \frac{1}{(2\pi)^3} \frac{k_n^2}{k^2-k_n^2} \int \frac{\mathcal{P}(\vec{r})}{\varepsilon} e^{-i\vec{k}\cdot\vec{r}}d^3\vec{r}. \tag{B4}$$

We search for the observed signal field in the phase-matched direction, far from the interaction volume. Let $R=(X,Y,Z)$ be the local point of observation. The field $\mathcal{E}(\vec{R})$ emitted far from the interaction volume is obtained using Eqs. (B1) and (B4)

$$\mathcal{E}(\vec{R}) = \frac{1}{(2\pi)^3} \int \frac{\mathcal{P}(\vec{r})}{\varepsilon}d^3\vec{r} \int_{PP} \frac{k_n^2}{k^2-k_n^2} e^{i\vec{k}\cdot(\vec{R}-\vec{r})}d^3\vec{k}. \tag{B5}$$

The integration on $\vec{k}$ is performed in cylindrical coordinates around the axis $\vec{R}-\vec{r}$ and by using the relation

$$\frac{1}{\pi} \int_{PP} \frac{e^{iKx}}{K}dK = i\,\text{sgn}(x) \tag{B6}$$

one obtains

$$\mathcal{E}(\vec{R}) = \frac{k_n^2}{4\pi\varepsilon} \int_V \frac{e^{ik_n|\vec{R}-\vec{r}|}+e^{-ik_n|\vec{R}-\vec{r}|}}{|\vec{R}-\vec{r}|}\mathcal{P}(\vec{r})d^3\vec{r}. \tag{B7}$$

Assuming that $R \gg r$, that is the Fraunhöffer approximation $r_\perp^2 \simeq r_x^2+r_y^2 \ll \lambda R$, one has $|\vec{R}-\vec{r}| \simeq R - \vec{r}\cdot\vec{R}/R$. We ignore the counterpropagating wave term in $e^{-ik_n|\vec{R}-\vec{r}|}$ since it is not phase matched and not observable in the forward direction, thus one obtains

$$\mathcal{E}(\vec{R}) = \frac{k_n^2}{4\pi\varepsilon R}e^{ik_nR} \int_V \mathcal{P}(\vec{r})e^{ik_n\vec{r}\cdot\vec{R}/R}d^3\vec{r}. \tag{B8}$$

This is the classical result, in other words, the field radiated at infinity in the $\vec{R}$ direction is the Fourier transform of $\mathcal{P}(\vec{r})$ with the wave vector $k_n\vec{R}/R$. At this step of the calculation, we have to calculate the total energy in the diffraction beam. The signal intensity is written as the flux of energy by surface unit and is expressed as

$$I(\vec{R}) = \frac{\varepsilon c}{2n}|\mathcal{E}(\vec{R})|^2. \tag{B9}$$

To provide the total signal intensity, Eq. (B9) is further integrated over the surface of the detector S_D, which corresponds to a particular solid angle Ω for signal emission

$$I_{\text{Sig}} = \int \int_{S_D} I(\vec{R})dXdY. \tag{B10}$$

It is developed as

$$I_{\mathrm{Sig}} = \frac{k_n^4 c}{32\pi^2 \varepsilon n} \int \int_{S_D} \left[\frac{dX dY}{R^2} \left| \right. \right.$$

$$\times \int \exp\left[-ik_n\left(\frac{X}{R}x + \frac{Y}{R}y + \frac{Z}{R}z\right) \right] \mathcal{P}(\vec{r}) dr^3 \left. \left| ^2 \right| \right]$$

$$= \frac{k_n^2 c}{32\pi^2 \varepsilon n} \int \int_\Omega \left[dK_x dK_y \left(\int \int_V \exp[-i(K_x x + K_y y \right. \right.$$

$$\left. + K_z z)] \mathcal{P}(x,y,z) dx dy dz \right)^2 \right], \tag{B11}$$

with $X/R = K_x/k_n$, $Y/R = K_y/k_n$ and $Z/R = K_z/k_n$ and $K_x^2 + K_y^2 + K_z^2 = k_n^2$. Equation (B11) is the final result. For any shape of the incoming beams and of the active volume, one can calculate $\mathcal{P}(x,y,z)$ in any point $\vec{r}$ and then evaluate numerically the five integrals, by choosing the solid angle around the phase-matched direction $\vec{k}_4$, but avoiding the directions of the incident beams.

We will now show that Eq. (B11) can be simplified to Eq. (53) if we use the same approximation as in the main text, i.e., if we assume plane waves and a cylindrical active area. Taking now z along $\vec{k}_4$ with $k_4 = k_n$ and using Eq. (46), one has

$$I_{\mathrm{Sig}} = \frac{k_n^2 c}{32\pi^2 \varepsilon n} \int \int_\Omega dK_x dK_y \int dK_z \delta(K_z - \sqrt{k_n^2 - K_x^2 - K_y^2})$$

$$\times \left[\int \int_S e^{K_x x + K_y y} P_{01}^{(4)} \int_0^L e^{i(k_n - K_z)z} dx dy dz \right]^2. \tag{B12}$$

Since $S \gg \lambda^2$, the diffraction angle Ω is small and $K_x, K_y \ll k_n$, then we simply have $K_z \simeq k_n$, leading to

$$I_{\mathrm{Sig}} = \frac{k_n^2 c}{32\pi^2 \varepsilon n} |P_{01}^{(4)}| L^2 \int \int_\Omega F_S^2(K_x, K_y) L_z^2 dK_x dK_y. \tag{B13}$$

F_S is the two-dimensional Fourier transform of the function $S(x,y) = 1$ within the surface S and zero outside, then applying the Parseval theorem

$$\int \int F_S^2(K_x, K_y) dK_x dK_y = 4\pi^2 \int \int S^2(x,y) dx dy$$

$$= 4\pi^2 S^2. \tag{B14}$$

Indeed since $F_S(K_x, K_y)$ is nonzero only for a very small solid angle, the integration can be extended to the full space and Eq. (B13) gives the same expression as Eq. (53) obtained by the simple method.

[1] V. Krüger, following paper, Phys. Rev. A **64**, 012717 (2001).
[2] R. L. Abrams and R. C. Lind, Opt. Lett. **2**, 94 (1978).
[3] R. L. Abrams and R. C. Lind, Opt. Lett. **3**, 205 (1978).
[4] B. Ai and R. J. Knize, J. Opt. Soc. Am. B **13**, 2408 (1996).
[5] D. Bloch and M. Ducloy, J. Opt. Soc. Am. **73**, 635 (1983).
[6] M. Ducloy, F. A. M. de Oliveira, and D. Bloch, Phys. Rev. A **32**, 1614 (1985).
[7] G. Grynberg, M. Pinard, and P. Verkerk, Opt. Commun. **50**, 261 (1984).
[8] G. Grynberg, M. Pinard, and P. Verkerk, J. Phys. (France) **47**, 617 (1986).
[9] J. Cooper et al., Phys. Rev. A **40**, 5705 (1989).
[10] D. R. Meacher, P. G. R. Smith, P. Ewart, and J. Cooper, Phys. Rev. A **46**, 2718 (1992).
[11] P. G. R. Smith and P. Ewart, Phys. Rev. A **54**, 2347 (1996).
[12] R. P. Lucht, R. L. Farrow, and D. J. Rakestraw, J. Opt. Soc. Am. B **10**, 1508 (1993).
[13] M. S. Brown, L. A. Rahn, and R. P. Lucht, Appl. Opt. **34**, 3274 (1995).
[14] T. A. Reichardt and R. P. Lucht, J. Opt. Soc. Am. B **13**, 2807 (1996).
[15] T. A. Reichardt and R. P. Lucht, J. Opt. Soc. Am. B **14**, 2449 (1997).
[16] T. A. Reichardt and R. P. Lucht, J. Chem. Phys. **109**, 5830 (1998).
[17] T. A. Reichardt and R. P. Lucht, J. Opt. Soc. Am. B **15**, 2566 (1998).
[18] T. A. Reichardt and R. P. Lucht, J. Opt. Soc. Am. B **13**, 1107 (1996).
[19] H. Bervas, S. Le Boiteux, B. Attal-Trétout, and J. P. Taran, J. Phys. B **25**, 469 (1992).
[20] H. Bervas, S. Le Boiteux, L. Labrunie, and B. Attal-Trétout, Mol. Phys. **79**, 911 (1993).
[21] T. A. Reichardt and R. P. Lucht, J. Chem. Phys. **111**, 10 008 (1999).
[22] B. Attal-Trétout et al., J. Phys. B **30**, 497 (1997).
[23] O. Blum, P. Harshman, T. K. Gustavson, and P. Kelley, Phys. Rev. A **47**, 5565 (1993).
[24] G. N. Robertson et al., J. Quant. Spectrosc. Radiat. Transf. **55**, 71 (1996).
[25] T. A. Wasserman, P. H. Vaccaro, and B. R. Johnson, J. Chem. Phys. **106**, 6314 (1997).
[26] T. Müller, T. A. Wasserman, P. H. Vaccaro, and B. R. Johnson, J. Chem. Phys. **108**, 4 (1998).
[27] T. A. Wasserman, P. H. Vaccaro, and B. R. Johnson, J. Chem. Phys. **108**, 7713 (1998).
[28] S. Williams, R. N. Zare, and L. A. Rahn, J. Chem. Phys. **101**, 1072 (1994).
[29] A. Omont, Prog. Quantum Electron. **5**, 69 (1977).
[30] M. Dumont and B. Decomps, J. Phys. (France) **29**, 181 (1968).
[31] A. Omont, Ph.D. thesis, Faculté des Sciences, Université de Paris, Paris, 1967.
[32] K. Blum, Density Matrix Theory and Applications (Plenum, New York, 1996).
[33] A. J. Orr-Ewing and R. N. Zare, The Chemical Dynamics and Kinetics of Small Radicals, Vol. 6 of Advanced Series in Physical Chemistry (World Scientific, Singapore, 1994).
[34] M. D. Levenson and S. S. Kano, Introduction to Nonlinear

Laser Spectroscopy (Academic Press, New York, 1987).

[35] M. Dumont, Ph.D. thesis, Université Paris, 1971.

[36] G. Herzberg, *Molecular Spectra and Molecular Structure, Spectra of Diatomic Molecules* (D. Van Nostrand, Princeton, 1950).

[37] C. Amiot, R. Bacis, and G. Guelachvili, Can. J. Phys. **56**, 251 (1978).

[38] C. Amiot and J. Verges, Phys. Scr. **26**, 422 (1982).

[39] B. Attal-Trétout, P. Monot, and K. Müller-Dethlefs, Mol. Phys. **73**, 1257 (1991).

[40] R. N. Zare, *Angular Momentum* (Wiley, New York, 1988).

[41] L. T. Earls, Phys. Rev. **48**, 423 (1935).

[42] S. Williams, L. A. Rahn, and R. N. Zare, J. Chem. Phys. **104**, 3947 (1996).

[43] A. Y. Chang, M. D. D. Rosa, and R. K. Hanson, J. Quant. Spectrosc. Radiat. Transf. **47**, 375 (1992).

[44] M. D. D. Rosa and R. K. Hanson, J. Quant. Spectrosc. Radiat. Transf. **52**, 515 (1994).

[45] K. Kohse-Höinghaus, Prog. Energy Combust. Sci. **20**, 203 (1994).

[46] N. L. Garland *et al.*, J. Chem. Phys. **84**, 4970 (1986).

[47] M. Ducloy and M. Dumont, J. Phys. (France), **31**, 419 (1970).

[48] D. Robert, P. Joubert, and B. Lance, J. Mol. Struct. **517-518**, 393 (2000).

[49] M. Islam, I. W. M. Smith, and J. W. Wiebrecht, J. Chem. Phys. **103**, 9676 (1995).

[50] A. S. Sudbø and M. M. T. Loy, J. Chem. Phys. **76**, 3646 (1982).

[51] X. Yang and A. M. Wodtke, J. Chem. Phys. **196**, 5123 (1992).

[52] W. G. Mallard, J. Miller, and K. C. Smyth, J. Chem. Phys. **76**, 3483 (1982).

[53] T. Ebata *et al.*, Chem. Phys. **84**, 151 (1984).

[54] J. W. Thoman Jr., J. A. Gray, J. L. Durant Jr., and P. H. Paul, J. Chem. Phys. **97**, 8156 (1992).

[55] P. H. Paul, J. A. Gray, J. L. Durant Jr., and J. W. Thoman Jr., Appl. Phys. B: Photophys. Laser Chem. **57**, 249 (1993).

[56] M. C. Drake and J. W. Ratcliffe, J. Chem. Phys. **98**, 3850 (1993).

[57] I. S. McDermid and J. B. Laudenslager, J. Quant. Spectrosc. Radiat. Transf. **27**, 483 (1982).

[58] R. J. Cattolica, T. G. Mataga, and J. A. Cavolowsky, J. Quant. Spectrosc. Radiat. Transf. **42**, 499 (1989).

[59] P. M. Danehy, E. J. Friedmann-Hill, R. P. Lucht, and R. L. Farrow, Appl. Phys. B: Photophys. Laser Chem. **57**, 243 (1993).

[60] S. Williams, R. N. Zare, and L. A. Rahn, J. Chem. Phys. **101**, 1093 (1994).

[61] A. Kumar, C.-C. Hsiao, Y.-Y. Lee, and Y.-P. Lee, Chem. Phys. Lett. **297**, 300 (1998).